



THE UNIVERSITY *of* EDINBURGH

## Edinburgh Research Explorer

### **Neonatal morphometric similarity mapping for predicting brain age and characterizing neuroanatomic variation associated with preterm birth**

**Citation for published version:**

Galdi, P, Blesa, M, Stoye, DQ, Sullivan, G, Lamb, GJ, Quigley, AJ, Thrippleton, MJ, Bastin, ME & Boardman, JP 2020, 'Neonatal morphometric similarity mapping for predicting brain age and characterizing neuroanatomic variation associated with preterm birth', *NeuroImage: Clinical*, vol. 25, 102195.  
<https://doi.org/10.1016/j.nicl.2020.102195>

**Digital Object Identifier (DOI):**

[10.1016/j.nicl.2020.102195](https://doi.org/10.1016/j.nicl.2020.102195)

**Link:**

[Link to publication record in Edinburgh Research Explorer](#)

**Document Version:**

Version created as part of publication process; publisher's layout; not normally made publicly available

**Published In:**

NeuroImage: Clinical

**General rights**

Copyright for the publications made accessible via the Edinburgh Research Explorer is retained by the author(s) and / or other copyright owners and it is a condition of accessing these publications that users recognise and abide by the legal requirements associated with these rights.

**Take down policy**

The University of Edinburgh has made every reasonable effort to ensure that Edinburgh Research Explorer content complies with UK legislation. If you believe that the public display of this file breaches copyright please contact [openaccess@ed.ac.uk](mailto:openaccess@ed.ac.uk) providing details, and we will remove access to the work immediately and investigate your claim.



## Journal Pre-proof

Neonatal morphometric similarity mapping for predicting brain age and characterizing neuroanatomic variation associated with preterm birth

Paola Galdi, Manuel Blesa, David Q. Stoye, Gemma Sullivan, Gillian J. Lamb, Alan J. Quigley, Michael J. Thrippleton, Mark E. Bastin, James P. Boardman

PII: S2213-1582(20)30032-2  
DOI: <https://doi.org/10.1016/j.nicl.2020.102195>  
Reference: YNICKL 102195



To appear in: *NeuroImage: Clinical*

Received date: 23 October 2019  
Revised date: 14 January 2020  
Accepted date: 21 January 2020

Please cite this article as: Paola Galdi, Manuel Blesa, David Q. Stoye, Gemma Sullivan, Gillian J. Lamb, Alan J. Quigley, Michael J. Thrippleton, Mark E. Bastin, James P. Boardman, Neonatal morphometric similarity mapping for predicting brain age and characterizing neuroanatomic variation associated with preterm birth, *NeuroImage: Clinical* (2020), doi: <https://doi.org/10.1016/j.nicl.2020.102195>

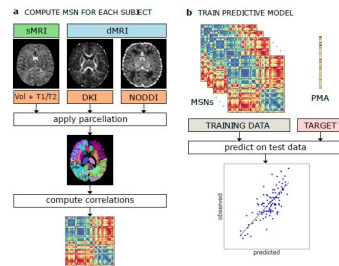
This is a PDF file of an article that has undergone enhancements after acceptance, such as the addition of a cover page and metadata, and formatting for readability, but it is not yet the definitive version of record. This version will undergo additional copyediting, typesetting and review before it is published in its final form, but we are providing this version to give early visibility of the article. Please note that, during the production process, errors may be discovered which could affect the content, and all legal disclaimers that apply to the journal pertain.

© 2020 Published by Elsevier Inc.  
This is an open access article under the CC BY-NC-ND license.  
(<http://creativecommons.org/licenses/by-nc-nd/4.0/>)

**Highlights**

- Multiple MRI features are integrated in a single model to study brain maturation in newborns.
- Morphometric similarity networks (MSNs) provide a whole-brain description of the structural properties of neonatal brain.
- The information encoded in MSNs is predictive of chronological brain age in the perinatal period.
- MSNs provide a novel data-driven method for investigating neuroanatomic variation associated with preterm birth.

## Graphical Abstract



# Neonatal morphometric similarity mapping for predicting brain age and characterizing neuroanatomic variation associated with preterm birth

Paola Galdi<sup>a,1,\*</sup>, Manuel Blesa<sup>a,1</sup>, David Q. Stoye<sup>a</sup>, Gemma Sullivan<sup>a</sup>, Gillian J. Lamb<sup>a</sup>, Alan J. Quigley<sup>b</sup>, Michael J. Thrippleton<sup>c,d</sup>, Mark E. Bastin<sup>c</sup>, James P. Boardman<sup>a,c</sup>

<sup>a</sup>MRC Centre for Reproductive Health, University of Edinburgh, Edinburgh EH16 4TJ, UK

<sup>b</sup>Department of Radiology, Royal Hospital for Sick Children, Edinburgh EH9 1LF, UK

<sup>c</sup>Centre for Clinical Brain Sciences, University of Edinburgh, Edinburgh EH16 4SB, UK

<sup>d</sup>Edinburgh Imaging, University of Edinburgh, Edinburgh EH16 4SB, UK

## Abstract

Multi-contrast MRI captures information about brain macro- and micro-structure which can be combined in an integrated model to obtain a detailed “fingerprint” of the anatomical properties of an individual’s brain. Inter-regional similarities between features derived from structural and diffusion MRI, including regional volumes, diffusion tensor metrics, neurite orientation dispersion and density imaging measures, can be modelled as morphometric similarity networks (MSNs). Here, individual MSNs were derived from 105 neonates (59 preterm and 46 term) who were scanned between 38 and 45 weeks postmenstrual age (PMA). Inter-regional similarities were used as predictors in a regression model of age at the time of scanning and in a classification model to discriminate between preterm and term infant brains. When tested on unseen data, the regression model predicted PMA at scan with a mean absolute error of  $0.70 \pm 0.56$  weeks, and the classification model achieved 92% accuracy. We conclude that MSNs predict chronological brain age accurately; and they provide a data-driven approach to identify networks that characterise typical maturation and those that contribute most to neuroanatomic variation associated with preterm

\*Correspondence: Paola Galdi, Queen’s Medical Research Institute, 47 Little France Crescent, Edinburgh EH16 4TJ, UK. Email: paola.galdi@ed.ac.uk

<sup>1</sup>These authors contributed equally to the work.

birth.

*Keywords:* morphometric similarity networks, preterm, developing brain, brain age, multi-modal data, MRI

---

## Highlights

1. Multiple MRI features are integrated in a single model to study brain maturation in newborns.
2. Morphometric similarity networks (MSNs) provide a whole-brain description of the structural properties of neonatal brain.
3. The information encoded in MSNs is predictive of chronological brain age in the perinatal period.
4. MSNs provide a novel data-driven method for investigating neuroanatomic variation associated with preterm birth.

## 1. Introduction

Preterm birth is closely associated with increased risk of neurodevelopmental, cognitive and psychiatric impairment that extends across the life course (Nosarti et al., 2012; Anderson, 2014; Mathewson et al., 2017; Van Lieshout et al., 2018). Structural and diffusion MRI (sMRI and dMRI) support the conceptualisation of atypical brain growth after preterm birth as a process characterised by micro-structural alteration of connective pathways due to impaired myelination and neuronal dysmaturation (Boardman et al., 2006; Anjari et al., 2007; Counsell et al., 2008; Ball et al., 2013b; Back and Miller, 2014; Van Den Heuvel et al., 2015; Eaton-Rosen et al., 2015; Thompson et al., 2016; Batalle et al., 2017; Telford et al., 2017; Batalle et al., 2018); this leads to a “dysconnectivity phenotype” that could form the basis for long term functional impairment (Boardman et al., 2010; Caldinelli et al., 2017; Keunen et al., 2017; Cao et al., 2017; Batalle et al., 2018b). However, there has not been a unified approach that incorporates information from sMRI and dMRI to study brain maturation

16 in the perinatal period so the set of image features that best capture brain  
17 maturation, and support image classification, are unknown.

18 The majority of neonatal connectomics studies have used single modes of  
19 data such as dMRI tractography (Brown et al., 2014; Bataille et al., 2017; Blesa  
20 et al., 2019) or resting-state functional connectivity (Ball et al., 2016; Smyser  
21 et al., 2016a). An alternative connectome model is the structural covariance  
22 network (SCN) approach (Alexander-Bloch et al., 2013) in which covariance be-  
23 tween regional measurements is calculated across subjects, resulting in a single  
24 network for the entire population. Other approaches have constructed subject-  
25 specific SCNs (Li et al., 2017; Mahjoub et al., 2018) or higher order morpho-  
26 logical networks to model the relationship between ROIs across different views  
27 (Soussia and Rekik, 2018), but these techniques have been restricted to the use  
28 of morphometric variables available through standard structural T1-weighted  
29 MRI sequences and by using a single metric (e.g. cortical thickness) to assess  
30 the “connectivity” between nodes (Shi et al., 2012).

31 Based on observations that integrating data from different MRI sequences  
32 enhances anatomic characterization (Melbourne et al., 2014; Kulikova et al.,  
33 2015; Ball et al., 2017; Thompson et al., 2018a), we investigated whether whole-  
34 brain structural connectomes derived from multi-modal data within a prediction  
35 framework can capture novel information about perinatal brain development.  
36 We used morphometric similarity networks (MSNs) to model inter-regional cor-  
37 relations of multiple macro- and micro-structural multi-contrast MRI variables  
38 in a single individual. This approach was originally devised to study how hu-  
39 man cortical networks underpin individual differences in psychological functions  
40 (Seidlitz et al., 2018), and we adapted it to describe both cortical and subcor-  
41 tical regions in the developing brain. The method works by computing for  
42 each region of interest (ROI) a number of metrics derived from different MRI  
43 sequences which are arranged in a vector. The aim is to obtain a multidimen-  
44 sional description of the structural properties of the ROIs. The MSN is then  
45 built considering the ROIs as nodes and modelling connection strength as the  
46 correlation between pairs of ROI vectors, thus integrating in a single connectome

the ensemble of imaging features. The pattern of inter-regional correlations can be conceptualised as a “fingerprint” of an individual’s brain.

We investigated the utility of MSNs for describing brain maturation, and for patient classification. The edges of individual MSNs were used to train two predictive models: a regression model to predict postmenstrual age (PMA) at scan and identify the set of image features that best model chronological brain age; and a classification model to discriminate between preterm infants at term equivalent age and term neonates, and thereby identify the networks that explain neuroanatomic variation associated with preterm birth. We hypothesized that predictive models based on MSNs, which integrate information from multiple data modalities, would outperform models based on single metrics and single data modalities.

## 2. Material and methods

### 2.1. Participants and data acquisition

Participants were recruited as part of a longitudinal study designed to investigate the effects of preterm birth on brain structure and long term outcome. The study was conducted according to the principles of the Declaration of Helsinki, and ethical approval was obtained from the UK National Research Ethics Service. Parents provided written informed consent. One hundred and twelve neonates underwent MRI at term equivalent age at the Edinburgh Imaging Facility: Royal Infirmary of Edinburgh, University of Edinburgh, UK, and 105 had multi-modal imaging suitable for MSN analysis (7 acquisitions did not yield usable datasets across all modalities due to motion or wakefulness during one or more sequences). The study group contained 46 term and 59 preterm infants (details are provided in Table 1). The distribution of PMA at scan for all participants, for the term and preterm groups, and the distribution by gender are shown in Fig. 1. Of the preterm infants, 12 had bronchopulmonary dysplasia, 3 had necrotising enterocolitis and 3 required treatment for retinopathy of prematurity.



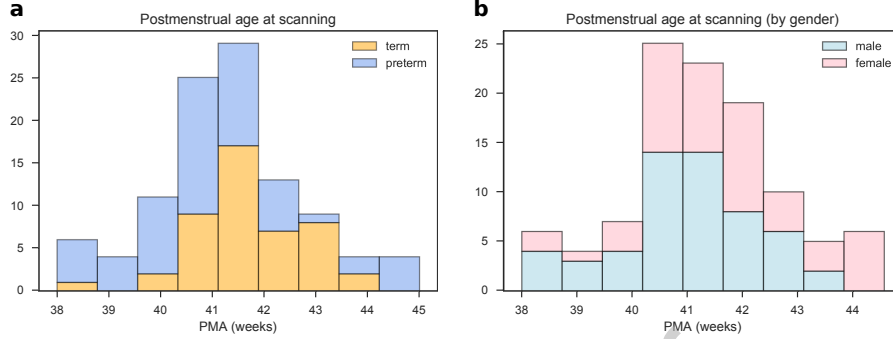


Figure 1: Distribution of postmenstrual age at scan for all subjects. a) Age distribution for the for term (blue) and preterm (orange) groups. b) Age distribution for male (blue) and female (pink) participants.

Table 1: Participant characteristics. The last column reports the  $p$  values of the group differences computed with the Wilcoxon rank-sum test for continuous variables and with the chi-squared test for categorical variables.

	preterm (N=59)	term (N=46)	all (N=105)	preterm vs. term
PMA at birth (weeks)	23.42-32.00	37.00-42.00	23.42-42.00	$p = 1.88 \times 10^{-18}$
Birth weight (grams)	454-2100	2556-4560	454-4560	$p = 1.93 \times 10^{-18}$
PMA at scan (weeks)	38.00-44.56	38.28-43.84	38.00-44.56	$p = 0.0035$
M:F ratio	29:30	26:20	55:50	$p = 0.4532$

PMA = Postmenstrual age, M = male, F = female.

76 A Siemens MAGNETOM Prisma 3 T MRI clinical scanner (Siemens Health-  
 77 care Erlangen, Germany) and 16-channel phased-array paediatric head coil were  
 78 used to acquire: 3D T1-weighted MPRAGE (T1w) (acquired voxel size = 1mm  
 79 isotropic) with TI 1100 ms, TE 4.69 ms and TR 1970 ms; 3D T2-weighted  
 80 SPACE (T2w) (voxel size = 1mm isotropic) with TE 409 ms and TR 3200 ms;  
 81 and axial dMRI. dMRI was acquired in two separate acquisitions to reduce the  
 82 time needed to re-acquire any data lost to motion artefact: the first acquisition  
 83 consisted of 8 baseline volumes ( $b = 0$  s/mm<sup>2</sup> [b0]) and 64 volumes with  $b =$   
 84 750 s/mm<sup>2</sup>, the second consisted of 8 b0, 3 volumes with  $b = 200$  s/mm<sup>2</sup>, 6  
 85 volumes with  $b = 500$  s/mm<sup>2</sup> and 64 volumes with  $b = 2500$  s/mm<sup>2</sup>; an op-  
 86 timal angular coverage for the sampling scheme was applied (Caruyer et al.,

2013). In addition, an acquisition of 3 b0 volumes with an inverse phase encoding direction was performed. All dMRI images were acquired using single-shot spin-echo echo planar imaging (EPI) with 2-fold simultaneous multislice and 2-fold in-plane parallel imaging acceleration and 2 mm isotropic voxels; all three diffusion acquisitions had the same parameters (TR/TE 3400/78.0 ms).

Infants were fed and wrapped and allowed to sleep naturally in the scanner. Feeds were timed to increase the likelihood of post-prandial sleep, flexible earplugs and neonatal earmuffs (MiniMuffs, Natus) were used for acoustic protection, and a soothing environment was created in terms of light and noise. Pulse oximetry, electrocardiography and temperature were monitored. All scans were supervised by a doctor or nurse trained in neonatal resuscitation. Each acquisition was inspected contemporaneously for motion artefact and repeated if there had been movement but the baby was still sleeping; dMRI acquisitions were repeated if signal loss was seen in 3 or more volumes. The majority of the cohort had one or more sequences repeated in order to acquire the best possible quality data for processing.

Conventional images were reported by an experienced paediatric radiologist (A.J.Q.) using a structured system (Leuchter et al., 2014; Woodward et al., 2006), and none of the images included in the final sample ( $N = 105$ ) showed evidence of focal parenchymal injury (defined as post-haemorrhagic ventricular dilatation, porencephalic cyst or cystic periventricular leukomalacia), or central nervous system malformation.

## 2.2. Data preprocessing

All the following preprocessing steps, including maps calculation and quality check, were performed using dcm2niix, FSL, MRtrix, MIRTk, ANTs, Connectome Workbench and cuDIMOT (Smith et al., 2004; Avants et al., 2011; Marcus et al., 2011; Makropoulos et al., 2014; Li et al., 2016; Hernandez-Fernandez et al., 2019; Tournier et al., 2019).

First, all DICOM image files (dMRI and sMRI) were converted to NIFTI (Li et al., 2016). Structural data were preprocessed using the developing Human

Connectome Project (dHCP) minimal structural processing pipeline for neonatal data (Makropoulos et al., 2018). Briefly, the T1w image was co-registered to the T2w image, both were corrected for bias field inhomogeneities (Tustison et al., 2010) and an initial brain mask was created (Smith, 2002). Following this, the brain was segmented into different tissue types (CSF: cerebrospinal fluid; WM: white matter; cGM: cortical grey matter; GM: subcortical grey matter) using the Draw-EM algorithm (Makropoulos et al., 2014). Twenty manually labelled atlases (Gousias et al., 2012) were then registered to each subject using a multi-channel registration approach, where the different channels of the registration were the original intensity T2-weighted images and GM probability maps. These GM probability maps were derived from an initial tissue segmentation, performed using tissue priors propagated through registration of a preterm probabilistic tissue atlas (Serag et al., 2012). The framework produces several output files, but for this study only the aligned T1w and the T2w images and the parcellation in 87 ROIs were used (Makropoulos et al., 2018). Note that from these 87 ROIs six were removed: the background, the unlabelled brain area (mainly internal capsule), the CSF, the lateral ventricles (left and right) and the corpus callosum (see section 2.4).

Diffusion MRI processing was performed as follows: for each subject the two dMRI acquisitions were first concatenated and then denoised using a Marchenko-Pastur-PCA-based algorithm (Veraart et al., 2016,b); the eddy current, head movement and EPI geometric distortions were corrected using outlier replacement and slice-to-volume registration with TOPUP and EDDY (Andersson et al., 2003; Smith et al., 2004; Andersson and Sotiropoulos, 2016; Andersson et al., 2016, 2017); bias field inhomogeneity correction was performed by calculating the bias field of the mean b0 volume and applying the correction to all the volumes (Tustison et al., 2010). This framework only differs from the optimal pipeline for diffusion preprocessing presented in Maximov et al. (2019) in that we did not perform the final smoothing or the gibbs-ring removal (Kellner et al., 2016) due to the nature of the data (partial fourier space acquisition).

The mean b0 EPI volume of each subject was co-registered to their structural

148 T2w volume using boundary-based registration (Greve and Fischl, 2009), then  
 149 the inverse transformation was used to propagate ROI labels to dMRI space,  
 150 with a modified bbrslope parameter of 0.5, which is used for neonatal data  
 151 (Toulmin et al., 2015).

152 For each ROI, two metrics were computed in structural space: ROI volume  
 153 and the mean T1w/T2w signal ratio (Glasser and Van Essen, 2011). The other  
 154 ten metrics were calculated in native diffusion space: five metrics derived from  
 155 the diffusion kurtosis (DK) model (Jensen et al., 2005) and five derived from the  
 156 Neurite Orientation Dispersion and Density Imaging model (NODDI) (Zhang  
 157 et al., 2012; Tariq et al., 2016).

### 158 2.3. Feature extraction

#### 159 2.3.1. Structural metrics

160 ROI volumes were calculated without normalising for the whole brain vol-  
 161 ume, as they are used only to compute inter-regional similarities within subjects.  
 162 The mean T1w/T2w signal ratio was calculated before the bias field correction.  
 163 The T1w/T2w ratio was used because it enhances myelin contrast and math-  
 164 ematically cancels the signal intensity bias related to the sensitivity profile of  
 165 radio frequency receiver coils (Glasser and Van Essen, 2011).

#### 166 2.3.2. Diffusion kurtosis metrics

167 The diffusion kurtosis (DK) model is an expansion of the diffusion tensor  
 168 model. In addition to the diffusion tensor, the DK model quantifies the degree  
 169 to which water diffusion in biological tissues is non-Gaussian using the kurtosis  
 170 tensor. The reason for this is that the Gaussian displacement assumption un-  
 171 derlying the diffusion tensor breaks at high b-values (Jensen et al., 2005). On  
 172 the kurtosis component, we only focus on the mean value along all diffusion  
 173 directions.

174 The metrics obtained from the DK model for each ROI are the means of: the  
 175 fractional anisotropy (FA), mean, axial and radial diffusivity (MD, RD, AD) and  
 176 kurtosis (MK). The MK map quantifies the deviation from Gaussianity of water

177 molecule displacement and can reflect different degrees of tissue heterogeneity  
 178 (Steven et al., 2014).

### 179 2.3.3. NODDI metrics

180 We included NODDI metrics alongside the more commonly adopted diffu-  
 181 sion tensor measures as previous studies have shown that NODDI indices are  
 182 sensitive to underlying biological changes in the brain and provide more spe-  
 183 cific microstructural characteristics, in agreement with histology (Grussu et al.,  
 184 2017; Bataille et al., 2018).

185 For the NODDI measures, the Bingham distribution was employed (Tariq  
 186 et al., 2016) as it allows extra flexibility by describing fibre dispersion along  
 187 two orthogonal axes. From this NODDI implementation we obtain five metrics:  
 188 intracellular volume fraction ( $v_{ic}$ ), isotropic volume fraction ( $v_{iso}$ ), the orien-  
 189 tation dispersion index along the primary and secondary directions ( $ODI_P$  and  
 190  $ODI_S$ ) and the overall orientation dispersion index ( $ODI_{TOT}$ ).

191 One limitation of this model is that it requires fixing a value for the diffu-  
 192 sivity along the axons. However, optimal values for this parameter are region-  
 193 dependent (Karmacharya et al., 2018) and the default value may be suboptimal  
 194 for the neonatal population as it has been optimised using an adult cohort  
 195 (Zhang et al., 2012; Karmacharya et al., 2018). Several studies have been re-  
 196 porting NODDI values for neonates using default (or unspecified) parameters  
 197 (Bataille et al., 2018; Bastiani et al., 2018; Karmacharya et al., 2018) or modi-  
 198 fied ones (Kunz et al., 2014; Jelescu et al., 2015). As our goal was not to report  
 199 NODDI values for the different areas, and because of the lack of reference val-  
 200 ues for this population, we calculated NODDI maps using default parameters  
 201 (Bataille et al., 2018).

### 202 2.4. Data Quality Control

203 The parcellations obtained after the processing were visually inspected and  
 204 parcels corresponding to CSF and background parcels were excluded because  
 205 they do not represent brain tissue. We observed a poor segmentation of the

corpus callosum in part of the subjects, but we did not find any anomalies in the rest of the parcels. This effect could be caused by different factors: a) this area is problematic to segment due to the proximity to CSF and its small thickness (see for example Otsuka et al. (2019)); b) the framework we used was optimised for the dHCP data that have a very high resolution ( $0.5 \text{ mm}^3$  isotropic) and data quality, making the partial volume effect more noticeable in data with a resolution of  $1 \text{ mm}^3$ ; c) or susceptibility artifacts. Instead of removing the subjects with a poor segmentation, we decided to remove the corpus callosum from the model, aiming at maximising the number of subjects. As a result of the whole quality check, we include the whole population ( $N = 105$ ) and each network is composed of 81 nodes (ROIs).

For the dMRI data we use eddy QC (Bastiani et al., 2019). The quality control is performed at subject level and group level. Eddy QC provides several measures related to the rotation, translation and outliers of the images. In addition, it also computes the signal-to-noise (SNR) ratio maps of the  $b_0$  volumes and the contrast-to-noise (CNR) ratio maps for the different  $b$ -values. These maps can be used at group level to visualise the quality of the data (Bastiani et al., 2018). The results show that the overall quality of the data-set was good (Fig. 2). For eddy QC to work, we removed the  $b\text{-value} = 200 \text{ s/mm}^2$  only from the quality control. This is because the low number of volumes with this  $b$ -value sometimes leads the Gaussian process performed by eddy to produce a perfect fit, which makes the CNR maps unrealistic.

Fig. 2 shows two representative subjects, one from the top quartile of the SNR and CNR distributions (green star) and one from the bottom quartile (red star). In the first panel we can see where they are placed in terms of SNR and CNR over the overall population. The second panel shows the SNR maps (for the  $b_0$ ) and the CNR maps (for the rest of  $b$ -values). The bottom panel of the Fig. 2 shows the  $b_0$  before and after the processing of the selected subjects. It is possible to observe the effect of the different steps involved, such as the EPI geometric corrections or the bias field inhomogeneity correction. Supplementary Figs. S8 and S9 report the above results for the term and preterm population

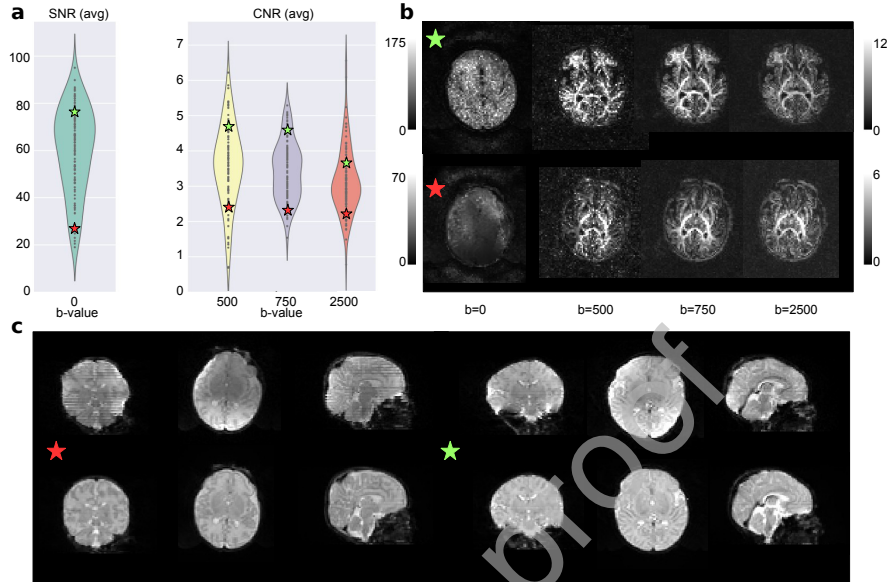


Figure 2: Quality control results. a) Results for the overall population with two selected subjects, one from the top quartile of the SNR and CNR distributions (green star) and the other from the bottom quartile (red star). b) The SNR and CNR maps for the selected subjects. c) The b0 of both subjects before and after the processing pipeline.

237 respectively.

238 Following Bastiani et al. (2019), for each volume, motion is quantified by  
 239 averaging voxel displacement across all voxels (computed as 3 translations and  
 240 3 rotations around the x, y and z axes). Absolute displacement is computed  
 241 with respect to the reference volume, while relative displacement is computed  
 242 with respect to the previous volume. A summary measure for each subject is  
 243 calculated as the average (absolute or relative) displacement across all volumes.  
 244 In Supplementary Fig. S10 we show the distribution of absolute and relative  
 245 motion for the term and the preterm groups. We compared the distributions  
 246 with a Wilcoxon rank-sum test and found no difference between the relative  
 247 motion scores ( $W = 1330$ ,  $p = 0.43$ ) and a significant difference between the  
 248 absolute motion scores ( $W = 1720$ ,  $p = 0.02$ ). However, as the violin plot  
 249 shows, this difference is driven by the presence of outliers.

## 250 2.5. *Experimental design and statistical analysis*

251 The models and the analyses described in this section were implemented in  
 252 Python (v3.6.4) using open source libraries and frameworks for scientific com-  
 253 puting, including SciPy (v1.0.0), Numpy (v1.14.0), Statsmodels (v0.8.0), Pan-  
 254 das (v0.22.0), Scikit-learn (v0.19.1) and Matplotlib (v2.1.2) (Jones et al., 2001;  
 255 Hunter, 2007; Seabold and Perktold, 2010; McKinney et al., 2010; Pedregosa  
 256 et al., 2011; Van Der Walt et al., 2011).

### 257 2.5.1. *Network Construction*

258 The MSN for each subject was constructed starting from 81 ROIs; each of the  
 259 ROI metrics was normalised (z-scored) and Pearson correlations were computed  
 260 between the vectors of metrics from each pair of ROIs. In this way, the nodes of  
 261 each network are the ROIs and the edges represent the morphometric similarity  
 262 between the two related ROIs (Fig. 3). In the following, the terms “edge”,  
 263 “connection” and “inter-regional similarity” are used interchangeably to refer  
 264 to the correlation between the regional metrics of a pair of ROIs.

### 265 2.5.2. *Confounding variables*

266 Early exposure to the extrauterine environment due to preterm birth ex-  
 267 poses infants to several processes that are known to impact brain maturation  
 268 (e.g. specific co-morbidities such as bronchopulmonary dysplasia and necrotis-  
 269 ing enterocolitis (Barnett et al., 2018)), and other processes and diseases that  
 270 can modify brain maturation (for example gestational age at birth, chorioam-  
 271 nionitis, fetal growth restriction, nutritional insufficiency, pain and medication  
 272 exposures (Duerden et al., 2016; Anblagan et al., 2016; Barnett et al., 2018;  
 273 Schneider et al., 2018; Duerden et al., 2018; Blesa et al., 2019)). In addition,  
 274 there may be as yet unknown environmental risks to brain structural connec-  
 275 tivity and genomic and epigenomic factors may interact with gestational age at  
 276 birth to confer risk (Batalle et al., 2017, 2018b; Boardman et al., 2014; Sparrow  
 277 et al., 2016; Krishnan et al., 2017). Therefore, it is not possible to define a  
 278 preterm infant cohort without any exposures to processes that could influence



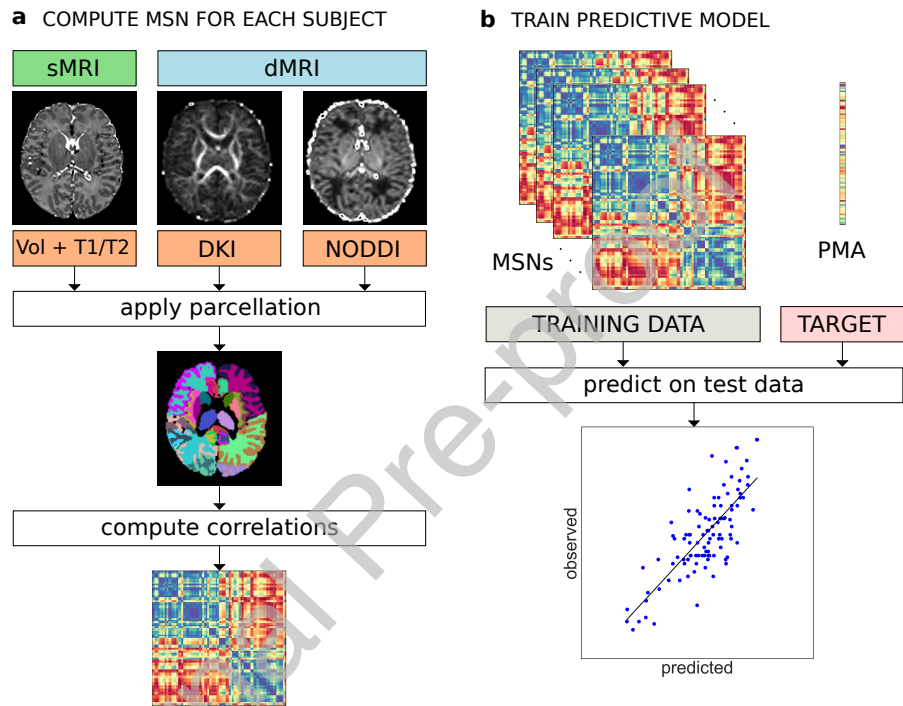


Figure 3: a) Individual MSN construction. Different metrics are extracted from dMRI and sMRI data. The same parcellation is applied to all image types and the average metric values are computed for each ROI. A MSN (represented here as a connectivity matrix) is built by computing the Pearson correlation between the vectors of metrics of each pair of ROIs. b) Training of a predictive model (here for PMA at scan) from individual MSNs. The inter-regional correlations are used as predictor variables in a machine learning model. The performance of the model is evaluated on an independent test set.

279 brain maturation. As our intention was to develop an integrated approach for  
 280 characterising dysmaturation in a study group representative of the target pop-  
 281 ulation, rather than to investigate possible drivers of dysmaturation, we did not  
 282 control for any of the above factors.

283 We did however find that the preterm group was characterised by higher in-  
 284 scanner motion than the term-group, hence we considered absolute displacement  
 285 as a confounder (section 2.4). We also observed a positive correlation ( $\rho =$   
 286  $0.27, p = 0.0048$ ) between PMA at scan and PMA at birth and a negative  
 287 correlation ( $\rho = -0.22, p = 0.0233$ ) between PMA at scan and gender (coded as  
 288 a binary variable where 0 indicates female infants and 1 male infants), implying  
 289 that in our sample term subjects and female subjects tend to have their scan  
 290 acquired at a later age (see also fig. 1). To control for potential bias, we  
 291 used these confounders as predictors and compared their predictive performance  
 292 with our network-based features. We tested the interaction between gender and  
 293 prematurity in a linear regression model of PMA at scan, but the interaction  
 294 term was not significant ( $p = 0.9634$ ). Birthweight was not included explicitly  
 295 as a confounder due to its collinearity with PMA at birth.

### 296 2.5.3. Regression model for age

297 We trained a linear regression model with elastic net regularisation to pre-  
 298 dict PMA at scan – i.e. chronological brain age – in both preterm and term  
 299 infants starting from individual MSNs. This model was chosen for its ability to  
 300 cope with a high number of features (Zou and Hastie, 2005). For each subject,  
 301 the edges of the MSN (inter-regional correlations) were concatenated to form a  
 302 feature vector to be given as input to the regression model. Since the connec-  
 303 tivity matrix representing the MSN is symmetric, we considered only the upper  
 304 triangular matrix for each subject. Gender and age at birth were included in the  
 305 model to control for their possible confounding effects. The prediction perfor-  
 306 mances were evaluated with a leave-one-out cross-validation (LOOCV) scheme,  
 307 by computing the mean absolute error (MAE) averaged across subjects. Within  
 308 each fold of the LOOCV, the parameters of the elastic net were selected with

309 a nested 3-fold cross-validation loop; the folds were stratified in percentiles to  
 310 include samples covering the whole age range in each of the folds. Permutation  
 311 testing was used for the statistical validation of the model performance: the null  
 312 distribution was built by running the age prediction analysis on 1000 random  
 313 permutation of the PMA.

#### 314 2.5.4. Classification model

315 A Support Vector Machine (SVM) classifier with linear kernel was trained  
 316 to discriminate between preterm and term infants. As per the regression model,  
 317 the input for each subject consisted of inter-regional connections taken from the  
 318 upper triangular connectivity matrix and the performances were evaluated with  
 319 LOOCV. Age at the time of scanning, gender and motion were included as ad-  
 320 ditional covariates. While in the case of regression the elastic net regularisation  
 321 performs automatically a variable selection step, recursive feature elimination  
 322 (RFE) was applied in combination with SVM to select the best subset of con-  
 323 nections. Model selection was implemented using nested cross validation: an  
 324 outer 3-fold cross-validation loop was used to select the SVM parameters and  
 325 an inner 4-fold cross-validation loop was used for RFE. Folds were stratified to  
 326 include the same proportion of term and preterm subjects. The accuracy of  
 327 the model was computed as the number of correctly classified subjects across  
 328 the leave-one-out folds over the total number of subjects in the test set. The  
 329 null distribution was built by repeating the exact same analysis 1000 times after  
 330 randomly assigning subjects to the term and the preterm group.

#### 331 2.5.5. Feature selection

332 After the preprocessing phase, twelve different metrics were available for each  
 333 ROI. To study which combination of features produced better performance in  
 334 the prediction tasks, we implemented a sequential backward-forward feature  
 335 selection scheme. Starting from the full set of features, at each iteration we  
 336 compare the performances of different models built by removing in turn each of  
 337 the features from the current set of candidate features. We then exclude from

the next iteration the feature whose subtraction caused the least increase in prediction error (down to three features, for a total of 73 combinations). The rationale behind this scheme is to explore the space of possible models without enumerating all possible solutions, thus reducing the computational demands compared to an exhaustive search. The procedure was performed separately for the regression and the classification models.

#### 2.5.6. Cross-validation strategy

We adopted LOOCV to select the best performing model in both the age prediction and the classification tasks as this scheme enabled maximum size of the training set and therefore best use of available data, but this strategy might induce high variance in the estimation of prediction accuracy (Kohavi, 1995; Efron, 1983). In the context of brain decoding (i.e. predictions from brain images or signals), LOOCV was shown to produce overly optimistic estimates of prediction accuracy in the within-subject setting (i.e. when all samples are highly correlated because they come from the same subject). In the between-subject setting (as in this work), the performance of LOOCV is similar to schemes involving random splits and mostly determined by sample size (Varoquaux et al., 2017; Varoquaux, 2018). To assess the stability of our results with respect to the chosen cross-validation scheme, we report the prediction accuracy computed with a 10 repeated stratified 5-fold scheme (10-5-fold) for all the models selected with LOOCV.

#### 2.5.7. Comparison with individual metrics and single data modalities models

We compared the performances of the best performing models based on MSNs with three classes of baseline models: a) models based on single global brain metrics (total brain volume and median FA in the WM); b) models based on individual metrics, where instead of similarities, predictors are the concatenation of all regional values for each of the individual metrics used to build MSNs; c) single data modality MSNs, i.e. models built on structural features only (Volume and T1/T2), on DKI features only, and on NODDI features only.

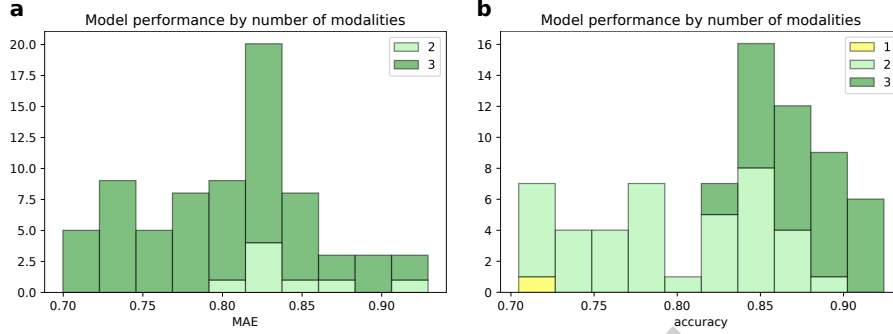


Figure 4: Histograms of the performance of the 73 models compared in the backward feature selection scheme for the age prediction task (a) and for the classification task (b). Bars are grouped by the number of modalities included in the models.

## 2.6. Data and code availability

Source code implementing the methods described in this paper is available upon request to the corresponding author. The preprocessed and anonymised data used in the analyses can be requested through the Brains Image Bank (<https://www.brainsimagebank.ac.uk/>) (Job et al., 2017).

## 3. Results

### 3.1. Feature selection

In Fig. 4 we report two histograms summarising the LOOCV performance of the 73 different models compared per each task in the backward feature selection scheme. In both cases, we can observe that the models based on all three data modalities achieved better results in terms of prediction accuracy. The performances of each of the compared model are reported in Supplementary Figs. S1 and S3 for the age prediction and for the classification models, respectively.

The best performing model for age prediction, which was adopted for all subsequent analyses, was based on seven features (Volume, FA, MD, AD, MK,  $v_{iso}$ ,  $ODI_P$ ). Fig. 5a shows the average MSN matrix computed across all subjects for the selected set of features and the matrix of correlation between inter-regional similarities and PMA at scan across subjects. The average MSN matrix shows

four main blocks that correspond roughly to positive correlations between ROIs within GM and between ROIs within WM, and to negative correlation between WM ROIs and GM ROIs, indicating that ROIs within GM (and within WM) share similar structural properties, while GM and WM regional descriptors tend to be anti-correlated. The four-block structure is recognisable also in the matrix reporting correlations with chronological age: with increasing age regions within GM or within WM become more similar with each other, while the dissimilarities between GM and WM ROIs increases.

The best classifier model was based on eleven out of the twelve features (all except  $ODI_S$ ), so compared to the age prediction model, four additional features were included: T1/T2, RD,  $v_{ic}$  and  $ODI_{TOT}$ . The average MSN computed with the selected features and the matrix of correlation with PMA at birth is shown in Fig. 5 (panels b and c). Comparing panel b and d of Fig. 5, it is apparent that while the patterns of correlation with PMA at scan and at birth are similar within GM and WM, subcortical ROIs show an opposite trend: with increasing PMA at scan subcortical ROIs tend to become more similar to WM ROIs and more dissimilar to GM ROIs, but the similarity between subcortical ROIs and cortical GM is positively correlated to age at birth.

### 3.2. Prediction results

The best regression model selected with LOOCV predicted chronological age (PMA at scan) with a MAE of  $0.70 \pm 0.56$  weeks on the test data, and a correlation between the predicted and the actual age equal to  $r = 0.78$  ( $p = 1.71 \times 10^{-22}$ ) (Supplementary Fig. S5). The results of the permutation test are shown in Fig. 6 and Supplementary Fig. S6. The confounding variables (gender and age at birth) were not selected by the internal feature selection procedure, hence the predictions were based on network features alone. To test whether there was any systematic difference in the predicted age between the term and the preterm group, we compared the error distributions with a Wilcoxon rank-sum test, but the result was not significant ( $W = 1108$ ,  $p = 0.1085$ ). For comparison, we evaluated the predictive performance of a linear regression model using

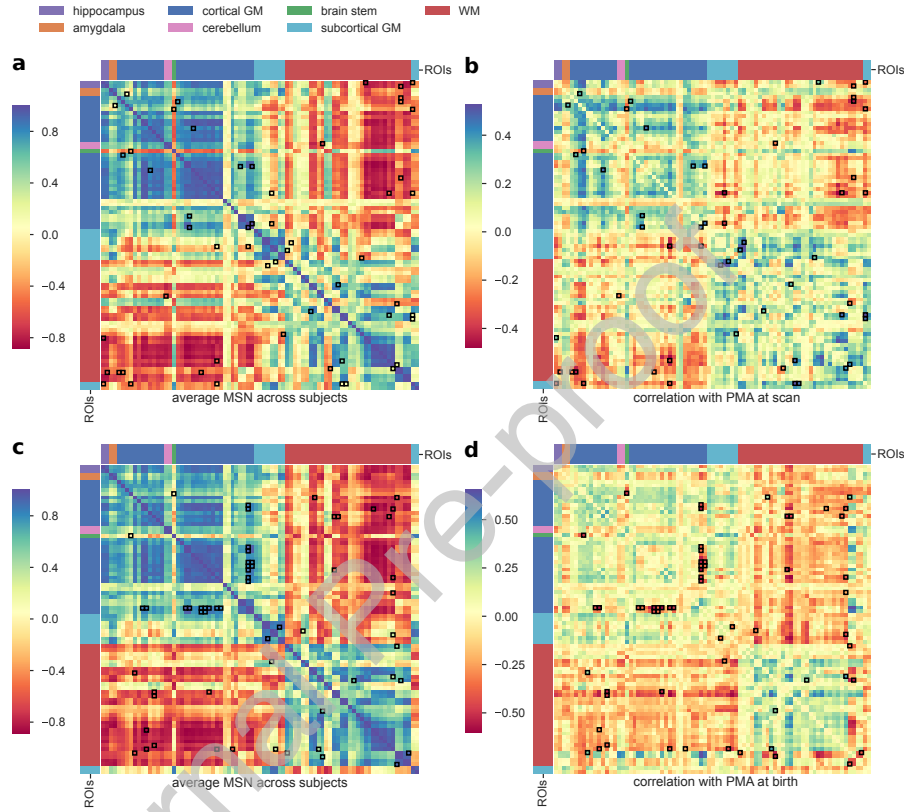


Figure 5: a) Average MSN computed across all subjects using the combination of features selected through the backward feature selection scheme for the age prediction task (Volume, FA, MD, AD, MK,  $v_{iso}$ ,  $ODI_P$ ). b) Correlation between each connection weight (inter-regional similarity) shown in (a) and PMA at scan across subjects. c) Average MSN computed across all subjects using the combination of features selected through the backward feature selection scheme for the classification task (Volume, T1/T2, FA, MD, AD, RD, MK,  $v_{ic}$ ,  $v_{iso}$ ,  $ODI_P$ ,  $ODI_{TOT}$ ). d) Correlation between each connection weight (inter-regional similarity) shown in (c) and PMA at birth across subjects. Connections that were identified as predictive features by the models are highlighted in black. ROIs are ordered as in Supplementary Table S1.

only gender and PMA at birth as independent variables, that achieved a MAE of  $1.03 \pm 0.88$  weeks. A Wilcoxon signed-rank test confirmed that the latter model achieved a significantly greater error ( $W = 1633$ ,  $p = 0.0001$ ). Also models based on single global metrics and single-modality MSNs models provided poorer predictive performance than the selected multi-modality MSNs model (brain volume: MAE=  $0.93 \pm 0.68$ ,  $R = 0.58$ ; median FA: MAE=  $0.88 \pm 0.63$ ,  $R = 0.58$ ; structural: MAE=  $1.08 \pm 0.79$ ,  $R = 0.32$ ; DKI: MAE=  $0.94 \pm 0.70$ ,  $R = 0.57$ ; NODDI: MAE=  $0.88 \pm 0.69$ ,  $R = 0.61$ ) and this was confirmed by a Wilcoxon signed-rank test (brain volume:  $W = 1813$ ,  $p = 0.0019$ ; median FA:  $W = 2045$ ,  $p = 0.0184$ ; structural:  $W = 1361$ ,  $p = 2.76 \times 10^{-06}$ ; DKI:  $W = 1734$ ,  $p = 0.0004$ ; NODDI:  $W = 1811$ ,  $p = 0.0009$ ). Conversely, the baseline model based on the ensemble on individual metrics used to build the best performing MSN model achieved similar performances (MAE:  $0.72 \pm 0.56$ ,  $R = 0.77$ ). A scatter plot of the residuals of the two models (Supplementary Fig. S11) showed a linear trend, indicating that the two models share a similar information content.

Supplementary Fig. S2 shows the results computed with 10-5-fold cross-validation in. All compared models performed similarly under the 10-5-fold scheme, and in general worse than with the LOOCV scheme, with the selected model achieving a MAE of  $1 \pm 0.2$  weeks (Supplementary Fig. S7).

To study which connections contributed the most to chronological age prediction, we selected only edges which were assigned a non-zero coefficient in at least 99% of cross-validation folds. These edges are shown in the chord diagram in Fig. 7 (realised with Circos, Krzywinski et al. (2009)), and are colour coded to distinguish between inter-regional similarities that increase or decrease with age, to highlight networks of regions whose morphological properties are converging (gray) or that tend to differentiate with increasing age (red). Intuitively, these edges connect ROIs whose anatomical and micro-structural properties are changing more than others between 38 and 45 weeks PMA, making the ROIs more or less similar. In other words, it is the relative timing of maturation of different brain tissues to determine the relevance of a connection in the age



prediction task. The selected connections are located in both cortical (frontal, temporal, parietal and occipital lobes; insular and posterior cingulate cortex) and subcortical regions (thalamus, subthalamic and lentiform nuclei), in the brain stem and in the cerebellum. These areas have been previously associated with age-related changes and preterm birth (Boardman et al., 2006; Ball et al., 2013a; Bataille et al., 2017). For comparison, we report in Supplementary Table S2 the regional metrics selected as most predictive of age in the baseline model based on individual metrics.

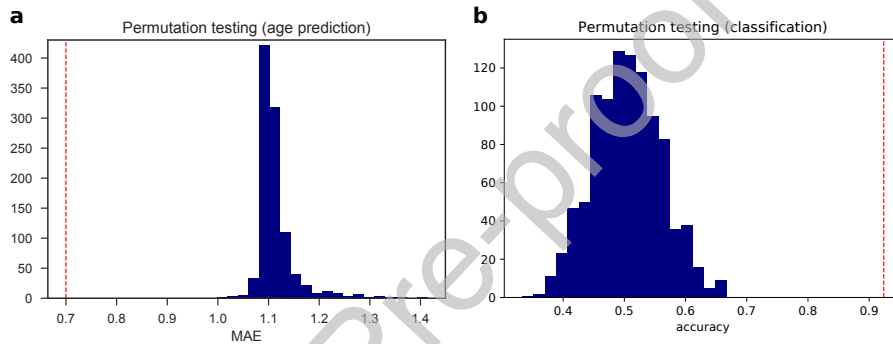


Figure 6: Null distributions computed over 1000 random permutations of the target variable for the age prediction (a) and the classification tasks (b). The red dotted lines indicate the performances of our models.

The best classifier discriminated between term and preterm infants with a 92% LOOCV accuracy (Fig. 6). None of the confounders were included among the selected features. A logistic regression model built on age at scan and gender did not achieve significant accuracy (56%,  $p = 0.091$ ), while adding motion to the predictors produced a 61% accuracy, slightly above chance level ( $p = 0.03$ ), but it should be noted that a model based on motion only was 59% accurate ( $p = 0.02$ ). Models based on global features achieved 55% accuracy for total brain volume and 56% accuracy for median FA. Models built on single data modalities attained 65% accuracy for structural features only, 89% accuracy for DKI features only, and 88% accuracy for NODDI features only. Results computed with 10-5-fold cross-validation are shown in Supplementary Fig. S4.

465 The best classifier selected with LOOCV also achieved top accuracy with 10-5-  
466 fold (accuracy 90%, Supplementary Fig. S7).

467 The network of regions that showed the most divergent pattern of structural  
468 brain properties in preterm versus term infants comprised the brain stem, the  
469 thalamus and the subthalamic nucleus; WM regions in the frontal and insu-  
470 lar lobes; GM regions in the occipital lobe; both WM and GM regions in the  
471 temporal and parietal lobes and in the posterior cingulate cortex. The chord  
472 diagram of edges selected by 99% of the models is shown in Fig. 8, in red where  
473 inter-regional similarities are greater in the term group and in gray where they  
474 are greater in the preterm group. For comparison, Supplementary Table S3 lists  
475 the regional metrics selected by the baseline model based on individual metrics,  
476 that obtained a 94% accuracy.

### 477 3.3. Testing for asymmetry

478 In both chord diagrams (Figs. 7 and 8) we observed more edges in the right  
479 hemisphere than in the left one. Both elastic net and SVM models perform a  
480 feature selection step to exclude features that are correlated and that carry re-  
481 dundant information in order to improve prediction performance, hence it might  
482 be the case that the models selected the right connections and discarded the  
483 left ones precisely because they had a similar information content. Additionally,  
484 in the leave-one-out cross-validation scheme the training sets only differ by two  
485 samples in each fold, hence models might be similar across folds.

486 To test the hypothesis that the two hemispheres carry a different information  
487 content, we performed two experiments. First, we repeated the same analyses  
488 extracting inter-regional similarities from either the right or the left hemisphere.  
489 We compared the performance obtained with the regression and classification  
490 models on the different subsets of features used in the backward feature se-  
491 lection scheme in the main analyses. We found that for the age prediction  
492 model a Wilcoxon signed-rank test testing the hypothesis that the prediction  
493 error was higher using only connections from the left hemisphere was significant  
494 ( $W = 156, p = 2.57 \times 10^{-11}$ ), while there was no statistically significant differ-

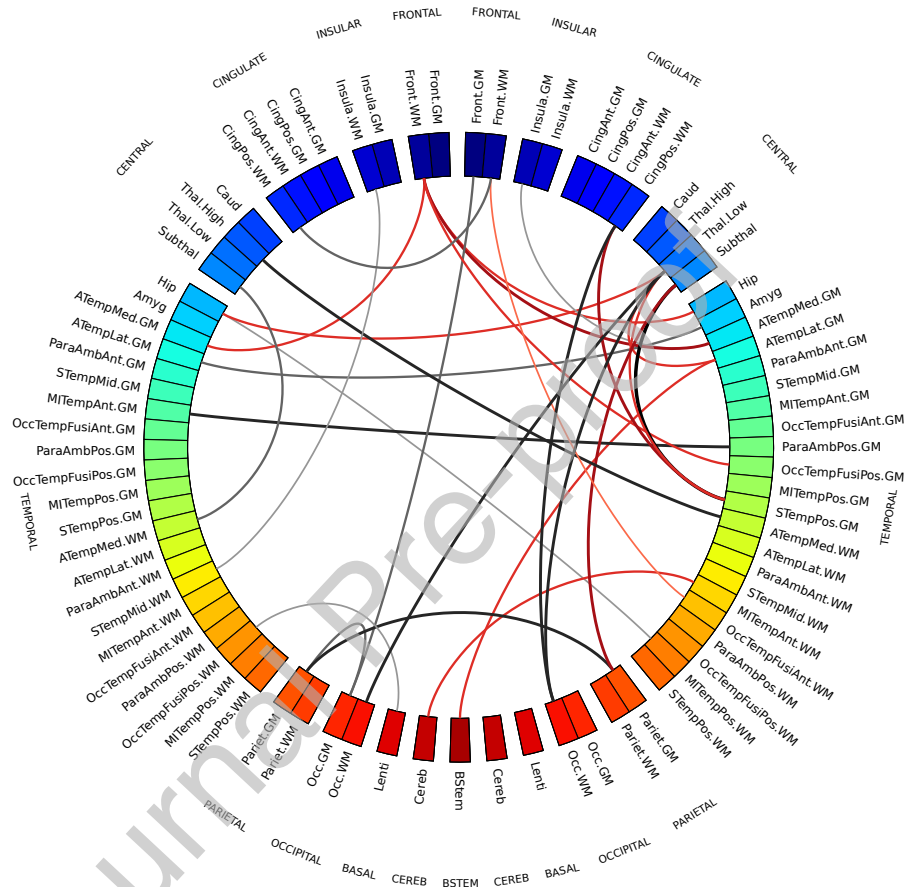


Figure 7: Chord diagram showing MSN edges used for age prediction in at least 99% of regression models in the cross-validation folds. Connections shown in gray are inter-regional similarities that increase with chronological age, while connections in red are inter-regional similarities that decrease with chronological age. The edge width is proportional to the correlation between inter-regional similarities and PMA. The left side of the diagram corresponds to the left side of the brain. Abbreviations for ROI names are explained in Supplementary Table S1.

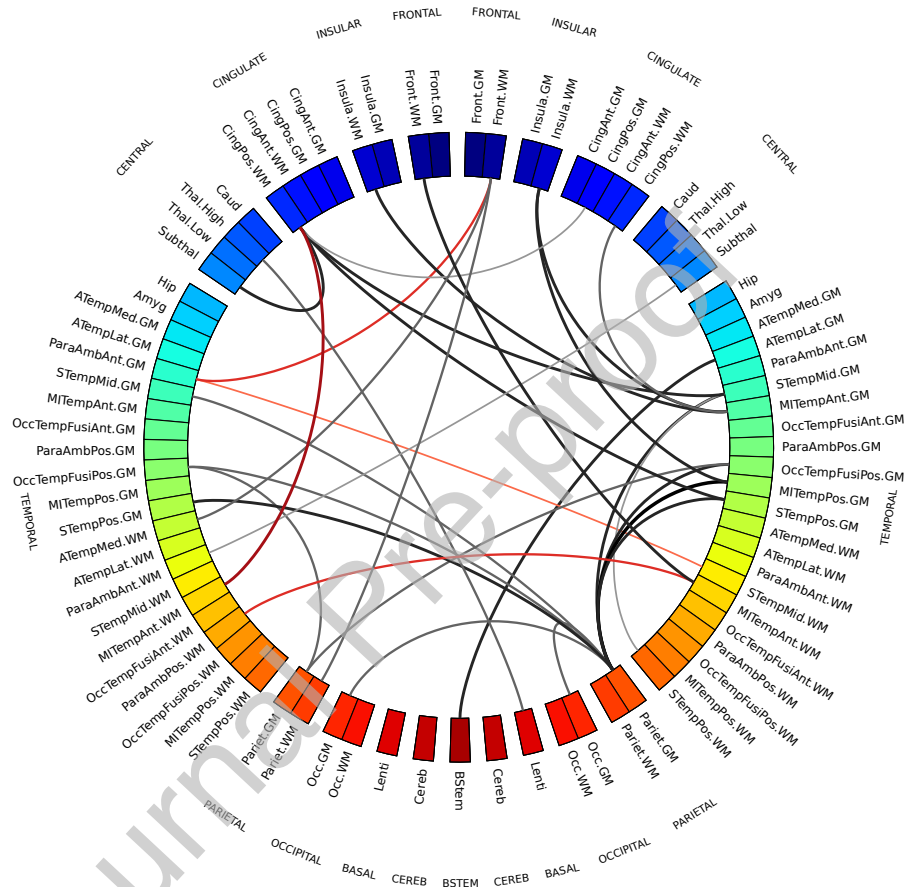


Figure 8: MSN edges showing a divergent pattern of morphological properties in term and preterm infants in at least 99% of classification models in the cross-validation folds. Gray connections indicate inter-regional similarities that are greater in the preterm group, while red connections are greater in the term group. The edge width is proportional to the correlation between inter-regional similarities and prematurity. The left side of the diagram corresponds to the left side of the brain. Abbreviations for ROI names are explained in Supplementary Table S1.

ence in the case of the classification model. These results replicated also when using 10-5-fold cross-validation (age prediction:  $W = 160, p = 2.98 \times 10^{-11}$ ; no significant difference in classification). We also compared the residuals obtained using either the right or the left hemisphere for age prediction with the set of features selected with backward feature selection (Supplementary Fig. S11) and found that the residuals of the fitted models are linearly correlated, suggesting that the two hemispheres do carry a similar information content, but one presents clearer signal than the other. We then used permutation testing to test the “interchangeability” of right and left regions: starting from the subsets of imaging metrics selected in the main analyses for the age prediction and classification models, we generated two null distributions by randomly swapping a subset of homotopic brain regions between the right and left hemisphere, and then repeating the exact same analyses 1000 times. We then counted how many times in the random models there was a disproportion of inter-regional similarities selected in the right hemisphere equal or greater than the one we observed with our models. If the right and left are “interchangeable”, the number of inter-regional similarities selected should remain the same on average. We found that in the age prediction task, under the null distribution, the disproportion of predictive connections in the right hemisphere was associated with a  $p = 0.036$ , while in the classification task the disproportion was not significant ( $p = 0.166$ ). This implies that at least for age prediction the two hemispheres are not interchangeable, suggesting again that the right hemisphere has a stronger signal. A similar trend was observed under the 10-5-fold cross-validation scheme, but in this case we could not reject the null hypothesis that inter-regional similarities are selected with the same frequency from both hemispheres ( $p = 0.098$ ).

#### 4. Discussion

These results show that the information encoded in MSNs is predictive of chronological brain age in the neonatal period and that MSNs provide a novel data-driven method for investigating neuroanatomic variation associated with

preterm birth. MSNs were built by combining features from different imaging sequences that describe complementary aspects of brain structure that have been previously studied in isolation (Makropoulos et al., 2016; Batalle et al., 2017) and the resulting predictive models achieved a high accuracy for age prediction and classification. By comparing the performance of MSNs features with basic demographic information (age at birth and gender) and simple metrics such as total brain volume and median white matter FA, we also showed that integrating imaging data provides relevant additional information to characterise brain age. Although we cannot exclude the possibility that some of the variability shared with age at birth, gender or brain volume is encoded in the imaging variables, the comparative analysis and the permutation testing results showed that the observed variance cannot be completely explained by demographic variables or simpler metrics alone. However, a high accuracy is not the only goal of the proposed method: once we have determined that the model is able to learn a relationship between the MSN features and age or prematurity, we can interrogate it to find out which features, regions and structures are involved in the predictions, thus allowing for further inferences.

We anticipate that the main clinical and research utilities of MSNs will be to investigate divergent maturational patterns in the context of perinatal environmental, genetic and clinical exposures, leading to improved understanding of antecedents to, and consequences of, atypical brain development. For these purposes a prediction tool with average 5 days error is highly precise compared with other methods for assessing brain maturation, which usually rely upon simple linear regression, use single image features, or broad classifications of prematurity (Toews et al., 2012; Brown et al., 2017; Batalle et al., 2018; Deprez et al., 2018; Bouyssi-Kobar et al., 2018; Ouyang et al., 2018).

The regions identified as most predictive have been previously associated with age-related changes and preterm birth (Boardman et al., 2006; Ball et al., 2013a; Batalle et al., 2017; Bouyssi-Kobar et al., 2018). These data suggest that to fully describe morphological variation in the developing brain it may be advantageous to adopt a holistic approach, leveraging the additional information

that can be derived from integrating multi-contrast MRI data. The main motivation for using a network-based approach is to obtain a whole-brain description of a developmental pattern. By using topologically integrated features instead of single metrics it is possible to access an additional layer of information that is not explicitly encoded in the individual metrics, i.e. how the relationships between metrics vary in different parts of the brain. Working with correlations instead of an ensemble of heterogeneous metrics also aids interpretation, as the focus is shifted from the values of single metrics across the brain, each influenced by disparate factors, to similarities between brain regions, which is a more relatable concept. Additionally, the adoption of a network model has proven to be a useful abstraction to capture the modular organisation of the brain: in the original work introducing MSNs to study microscale cortical organization in adults, the authors demonstrated that regions that were similar in MSNs were more likely to belong to the same cytoarchitectonic class, to be axonally connected and to have high levels of co-expressions of genes specialised for neural functions (Seidlitz et al., 2018). Another reason for working with similarities instead of single regional metrics is methodological: computing edge weights as inter-regional similarities enables an integrated representation of several metrics in a single network; to work with the original features directly would mean either working with several networks (thus requiring a further step to integrate them and aggravating the problems related with the “curse of dimensionality”) or concatenating all the features in a single predictive model (thus excluding the interactions between metrics from the model).

Table 2: Results from previous works in the age prediction task.

	Age span	Model	Error/Accuracy
Brown et al. 2017	27-45 weeks PMA	FA-weighted structural connectivity	MAE = 1.6 weeks
Ouyang et al. 2019	31.5-41.7 weeks PMA	cortical FA and MK (mean kurtosis)	FA: $r = .92$ ; MK: $r = .63$
Deprez et al. 2018	29-44 weeks PMA	spatio-temporal growth models for myelin-like signals in the thalami and brainstem	Thalami: MAE = 1.41 weeks Brainstem: MAE = 2.56 weeks
Toews et al. 2012	8-590 days from birth	scale-invariant T1w features	MAE = 72 days
Wu et al. 2019	14-48 days from birth	cortical measures	MAE = $11.1 \pm 0.3$ days

PMA = postmenstrual age, MAE = mean absolute error,  $r$  = Pearson’s coefficient between actual and predicted age.

Our data are consistent with previous studies of perinatal brain age prediction based on a single type of data or a single metric. For example, Brown et al. (2017) used dMRI tractography to predict brain dysmaturation in preterm infants with brain injury and abnormal developmental outcome and found that altered connectivity in the posterior cingulate gyrus and the inferior orbitofrontal cortex were associated with a delayed maturation; both of these regions are included in the networks identified by our model. Regional FA, MD, MK, and  $v_{ic}$  are each predictive of age (Genc et al., 2017; Karmacharya et al., 2018; Ouyang et al., 2019), and the first three measures were selected in our age prediction model. Growth of the thalami and brainstem, defined in terms of myelin-like signals from T2-weighted images, successfully predicted age between 29 and 44 weeks (Deprez et al., 2018) and these regions are included in the networks most predictive of age in the current study. In Toews et al. (2012), scale-invariant image features were extracted from T1-weighted MRI data of 92 subjects over an age range of 8-590 days to build a developmental model that was used to predict age of new subjects; and Ceschin et al. (2018) proposed a deep learning approach to detect subcortical brain dysmaturation from T2-weighted fast spin echo images in infants with congenital heart disease. Wu et al. (2019) used cortical features extracted from structural images to predict age of 50 healthy subjects with 251 longitudinal MRI scans from 14 to 797 days; in accordance with our results, the regions reported to be important for age prediction were bilateral medial orbitofrontal, parahippocampal, temporal pole, right superior parietal and posterior cingulate cortex. Although our results are not directly comparable with the above works because of the heterogeneity of employed models, validation techniques and population variation (different age ranges), our prediction error is among the lowest reported (see Table 2 for a summary of previous results), but it should be noted that there is a strong positive correlation between the reported MAEs and the age range of the samples. In addition, many works have identified imaging biomarkers associated with preterm birth, such as brain tissue volume (Alexander et al., 2018; Gui et al., 2019), myelin content (Melbourne et al., 2016), and diffusion tensor metrics (Anjari et al.,



2007; Bouyssi-Kobar et al., 2018).

The connections most predictive of age revealed that brain maturation is characterised by morphological convergence of some networks and divergence of others (Fig. 7). These connections mostly involve fronto-temporal and subcortical ROIs, which suggests that the micro- and macro-structural properties of these regions are highly dynamic between 38-45 weeks. Among these, inter-regional similarities within GM and WM increase with age, similarities between cortical GM and WM decrease, while subcortical ROIs become more similar to WM and more dissimilar to cortical GM. This is consistent with previous findings on the different trends in development of the thalamus and the cortex (Eaton-Rosen et al., 2015). Additionally, in a study of early development of structural networks (Batalle et al., 2017), connections to and from deep grey matter are reported to show the most rapid developmental changes between 25-45 weeks, while intra-frontal, frontal to cingulate, frontal to caudate and inter-hemispheric connections are reported to mature more slowly.

Conversely, the inter-regional similarities selected by the SVM classifier to discriminate between term and preterm (Fig. 5) are more distributed across cortical GM and WM and are for the most part greater in the preterm group. The fact that in the term group these cortical ROIs are less homogeneous in terms of structural properties could be interpreted as a sign that in term infants these regions are at a different stage of maturation where their morphological profile is consolidating along specialised developmental trajectories. It has been previously suggested that the rapid maturation of cortical structures occurring in the perinatal period is vulnerable to the effects of preterm birth (Kostović and Jovanov-Milošević, 2006; Ball et al., 2011, 2013b; Smyser et al., 2016b).

The differences between networks identified for age prediction and for preterm classification indicate that atypical brain development after preterm birth is not solely a problem of delayed maturation, but it is characterised by a specific signature. Indeed, while the age prediction networks capture changes occurring in both the preterm and the term group, the classification networks highlight where there are group-wise differences, and they do not match: in the case of a delayed

maturation we would have observed differences in the same regions undergoing age-related changes. MSN variations associated with preterm birth affected brain stem, thalami, sub-thalamic nuclei, WM regions in the frontal and insular lobes, GM regions in the occipital lobe, and WM and GM regions in the temporal and parietal lobes and in the posterior cingulate cortex. This distribution of structural variation is consistent with previous reports of regional alteration in brain volume and dMRI parameters based on single contrasts (Boardman et al., 2006; Bonifacio et al., 2010; Ball et al., 2013a; Brown et al., 2017; Batalle et al., 2017; Alexander et al., 2018; Thompson et al., 2018b; Bouyssi-Kobar et al., 2018). Furthermore, compared to the age prediction model, the MSNs used for preterm classification are based on four additional metrics: T1/T2, related to myelination; RD, measuring water dispersion;  $v_{ic}$  describing neurite density; and ODI<sub>TOT</sub>, associated with the fanning of WM tracts. All these metrics contribute to characterise the micro-structural alterations associated with preterm birth (Eaton-Rosen et al., 2015; Melbourne et al., 2016; Batalle et al., 2018; Thompson et al., 2018b; Bouyssi-Kobar et al., 2018).

We observed a disproportion in the distribution of the connections selected by our models, with a preference for the right hemisphere, hinting at the existence of lateralization in the maturational process. An asymmetry in the development of the right hemisphere in neonates was previously reported in Dubois et al. (2010); Yap et al. (2011); Wu et al. (2019), and our experiments (section 3.3) partially supported the hypothesis that the right hemisphere plays a relevant role in the context of age prediction.

#### 4.1. Limitations

This work has some limitations. First, compared with the original work on MSNs (Seidlitz et al., 2018), we did not have a multi-parametric mapping sequence (Weiskopf et al., 2013); however, because the model is extensible, information from other contrasts could be added and evaluated for their effect on prediction. The MSN model could also be applied to study the properties of cortical gray matter (such as thickness, sulcal depth or curvature), that have been

previously reported to be predictive of age in children (Brown et al., 2012) and could contribute significantly in characterising the newborn brain. However, metrics that only apply to selected structures (e.g. the cortex) cannot be used in a whole brain analysis, as to compute inter-regional similarities each region needs to be described by the same set of metrics. This particular study was designed based on prior knowledge that typical development and atypical development associated with preterm birth are characterised by global changes (Ball et al., 2013a; Anderson, 2014; Eaton-Rosen et al., 2015; Melbourne et al., 2014), and MSNs integrating dMRI and sMRI data were chosen to study generalised processes across the whole brain.

Second, we used a motion correction technique that attenuates the impact of head motion on structural connectivity (Andersson and Sotiropoulos, 2016; Baum et al., 2018), and we found that scanner motion was not contributing significantly to prediction accuracy; however we cannot rule out a possible confounding effect of motion on the estimation of regional metrics.

Third, the preterm study population was representative of survivors of modern neonatal intensive care in terms of gestational age range and prevalence of co-morbidities of preterm birth that may influence brain maturation, but it is still possible that the results were influenced by biological variability specific to the cohort. A replication study will be required to determine whether the patterns of dysmaturation we found are generalisable.

Finally, we assessed the performance of our models with both LOOCV and 10-5-fold schemes in order to investigate the stability of our findings with respect to the chosen cross-validation scheme and we observed some variability in the general trends of the results. The disagreement we found might derive from the limited size of the training set in the case of the repeated-5-fold scheme (all models tended to perform worse, suggesting there were not enough samples for learning), and this was indeed the reason why our first choice was the leave-one-out scheme. As it is always the case when working with machine learning, increasing the sample size would increase the power of the models, thereby reducing the margin of error and the risk of overfitting, with the result that

both schemes should converge to similar findings.

#### 4.2. Conclusions

Combining multiple imaging features in a single model enabled a detailed description of the morphological properties of the developing brain that was used inside a predictive framework to identify two networks of regions: the first, predominantly located in subcortical and fronto-temporal areas, that contributed most to age prediction: the second, comprising mostly frontal, parietal, temporal and insular regions, that discriminated between preterm and term born infant brains. Both predictive models performed best when structural, diffusion tensor-derived and NODDI metrics were combined, which demonstrates the importance of integrating different biomarkers to generate a global picture of the developing human brain. The achieved accuracy supports the hypothesis that studying the interaction between regional metrics can shed light on the mechanics of development.

Morphology, structural connectivity and maturation are all influenced by genetics, co-morbidities of preterm birth, and nutrition (Boardman et al., 2014; Anblagan et al., 2016; Sparrow et al., 2016; Krishnan et al., 2016; Ball et al., 2017; Alexander et al., 2018; Blesa et al., 2019). In future work MSNs could offer new understanding of the impact of these factors on integrated measures of brain development, and the relationship between neonatal MSNs and functional outcome could bring novel insights into the neural bases of cognition and behaviour, by identifying networks of regions associated with later development. MSNs could also enable a direct comparison with functional networks extracted from fMRI, to explore how structure and function interplay in the neonatal period, and study how well the two network models together explain individual variability in developmental outcome.

#### Conflicts of interest

Authors declare no conflict of interests.

## 729 Acknowledgements

730 We are grateful to the families who consented to take part in the study. This  
 731 work was supported by Theirworld ([www.theirworld.org](http://www.theirworld.org)) and was undertaken  
 732 in the MRC Centre for Reproductive Health, which is funded by MRC Centre  
 733 Grant (MRC G1002033). MJT was supported by NHS Lothian Research and  
 734 Development Office. Participants were scanned in the University of Edinburgh  
 735 Imaging Research MRI Facility at the Royal Infirmary of Edinburgh which was  
 736 established with funding from The Wellcome Trust, Dunhill Medical Trust, Ed-  
 737 inburgh and Lothians Research Foundation, Theirworld, The Muir Maxwell  
 738 Trust and many other sources; we thank the University's imaging research staff  
 739 for providing the infant scanning.

## 740 References

## 741 References

- 742 Alexander, B., Kelly, C.E., Adamson, C., Beare, R., Zannino, D., Chen, J.,  
 743 Murray, A.L., Loh, W.Y., Matthews, L.G., Warfield, S.K., Anderson, P.J.,  
 744 Doyle, L.W., Seal, M.L., Spittle, A.J., Cheong, J.L., Thompson, D.K., 2018.  
 745 Changes in neonatal regional brain volume associated with preterm birth and  
 746 perinatal factors. *NeuroImage* doi:10.1016/j.neuroimage.2018.07.021.
- 747 Alexander-Bloch, A., Giedd, J.N., Bullmore, E., 2013. Imaging structural co-  
 748 variance between human brain regions. *Nature Reviews Neuroscience* 14,  
 749 322–336. doi:10.1038/nrn3465.
- 750 Anblagan, D., Pataky, R., Evans, M.J., Telford, E.J., Serag, A., Sparrow, S.,  
 751 Piyasena, C., Semple, S.I., Wilkinson, A.G., Bastin, M.E., Boardman, J.P.,  
 752 2016. Association between preterm brain injury and exposure to chorioam-  
 753 nionitis during fetal life. *Scientific Reports* 6, 37932. doi:10.1038/srep37932.
- 754 Anderson, P.J., 2014. Neuropsychological outcomes of children born very  
 755 preterm. *Seminars in Fetal and Neonatal Medicine* 19, 90–96. doi:10.1016/  
 756 J.SINY.2013.11.012.

- 757 Andersson, J.L., Graham, M.S., Drobnjak, I., Zhang, H., Filippini, N., Bastiani,  
758 M., 2017. Towards a comprehensive framework for movement and distortion  
759 correction of diffusion MR images: Within volume movement. *NeuroImage*  
760 152, 450–466. doi:10.1016/j.neuroimage.2017.02.085.
- 761 Andersson, J.L., Graham, M.S., Zsoldos, E., Sotiropoulos, S.N., 2016. Incorporating outlier detection and replacement into a non-parametric framework  
762 for movement and distortion correction of diffusion MR images. *NeuroImage*  
763 141, 556–572. doi:10.1016/j.neuroimage.2016.06.058.
- 764 Andersson, J.L., Skare, S., Ashburner, J., 2003. How to correct susceptibility  
765 distortions in spin-echo echo-planar images: application to diffusion tensor  
766 imaging. *NeuroImage* 20, 870 – 888. doi:https://doi.org/10.1016/S1053-8119(03)00336-7.
- 767 Andersson, J.L., Sotiropoulos, S.N., 2016. An integrated approach to correction for off-resonance effects and subject movement in diffusion MR imaging.  
768 *NeuroImage* 125, 1063–1078. doi:10.1016/j.neuroimage.2015.10.019.
- 769 Anjari, M., Srinivasan, L., Allsop, J.M., Hajnal, J.V., Rutherford, M.A., Edwards, A.D., Counsell, S.J., 2007. Diffusion tensor imaging with tract-based  
770 spatial statistics reveals local white matter abnormalities in preterm infants.  
771 *NeuroImage* 35, 1021–1027. doi:10.1016/J.NEUROIMAGE.2007.01.035.
- 772 Avants, B.B., Tustison, N.J., Song, G., Cook, P.A., Klein, A., Gee, J.C., 2011. A  
773 reproducible evaluation of ants similarity metric performance in brain image  
774 registration. *NeuroImage* 54, 2033 – 2044. doi:https://doi.org/10.1016/j.neuroimage.2010.09.025.
- 775 Back, S.A., Miller, S.P., 2014. Brain injury in premature neonates: A primary  
776 cerebral dysmaturation disorder? *Annals of Neurology* 75, 469–486.
- 777 Ball, G., Aljabar, P., Arichi, T., Tusor, N., Cox, D., Merchant, N., Nongena, P.,  
778 Hajnal, J., Edwards, A., Counsell, S., 2016. Machine-learning to characterise

- 784 neonatal functional connectivity in the preterm brain. *NeuroImage* 124, 267–  
785 275. doi:10.1016/J.NEUROIMAGE.2015.08.055.
- 786 Ball, G., Aljabar, P., Nongena, P., Kennea, N., Gonzalez-Cinca, N., et al., 2017.  
787 Multimodal image analysis of clinical influences on preterm brain develop-  
788 ment. *Annals of Neurology* 82, 233–246. doi:10.1002/ana.24995.
- 789 Ball, G., Boardman, J.P., Aljabar, P., Pandit, A., Arichi, T., Merchant, N.,  
790 Rueckert, D., Edwards, A.D., Counsell, S.J., 2013a. The influence of preterm  
791 birth on the developing thalamocortical connectome. *Cortex* 49, 1711 – 1721.  
792 doi:<https://doi.org/10.1016/j.cortex.2012.07.006>.
- 793 Ball, G., Boardman, J.P., Rueckert, D., Aljabar, P., Arichi, T., Merchant, N.,  
794 Gousias, I.S., Edwards, A.D., Counsell, S.J., 2011. The effect of preterm birth  
795 on thalamic and cortical development. *Cerebral Cortex* 22, 1016–1024.
- 796 Ball, G., Srinivasan, L., Aljabar, P., Counsell, S.J., Durighel, G., Hajnal, J.V.,  
797 Rutherford, M.A., Edwards, A.D., 2013b. Development of cortical microstruc-  
798 ture in the preterm human brain. *Proceedings of the National Academy of*  
799 *Sciences* 110, 9541–9546. doi:10.1073/PNAS.1301652110.
- 800 Barnett, M.L., Tusor, N., Ball, G., Chew, A., Falconer, S., Aljabar, P., Kimpton,  
801 J.A., Kennea, N., Rutherford, M., David Edwards, A., Counsell, S.J., 2018.  
802 Exploring the multiple-hit hypothesis of preterm white matter damage using  
803 diffusion MRI. *NeuroImage: Clinical* 17, 596–606. doi:10.1016/J.NICL.  
804 2017.11.017.
- 805 Bastiani, M., Andersson, J., Cordero-Grande, L., Murgasova, M., Hutter, J.,  
806 Price, A.N., Makropoulos, A., Fitzgibbon, S.P., Hughes, E., Rueckert, D.,  
807 Victor, S., Rutherford, M., Edwards, A.D., Smith, S., Tournier, J.D., Hajnal,  
808 J.V., Jbabdi, S., Sotiropoulos, S.N., 2018. Automated processing pipeline for  
809 neonatal diffusion MRI in the developing human connectome project. *Neu-*  
810 *roImage* doi:<https://doi.org/10.1016/j.neuroimage.2018.05.064>.

- 811 Bastiani, M., Cottaar, M., Fitzgibbon, S.P., Suri, S., Alfaro-Almagro, F.,  
812 Sotiropoulos, S.N., Jbabdi, S., Andersson, J.L., 2019. Automated quality control for within and between studies diffusion MRI data using a non-parametric  
813 framework for movement and distortion correction. *NeuroImage* 184, 801 –  
814 812. doi:<https://doi.org/10.1016/j.neuroimage.2018.09.073>.
- 816 Batalle, D., Edwards, A.D., O’Muircheartaigh, J., 2018b. Annual research review: Not just a small adult brain: understanding later neurodevelopment through imaging the neonatal brain. *Journal of Child Psychology and Psychiatry* 59, 350–371. doi:10.1111/jcpp.12838.
- 820 Batalle, D., Hughes, E.J., Zhang, H., Tournier, J.D., Tusor, N., others., 2017. Early development of structural networks and the impact of prematurity on brain connectivity. *NeuroImage* 149, 379–392. doi:10.1016/j.neuroimage.2017.01.065.
- 824 Batalle, D., O’Muircheartaigh, J., Makropoulos, A., Kelly, C.J., Dimitrova, R., Hughes, E.J., Hajnal, J.V., Zhang, H., Alexander, D.C., Edwards, A.D., Counsell, S.J., 2018. Different patterns of cortical maturation before and after 38 weeks gestational age demonstrated by diffusion MRI in vivo. *NeuroImage* doi:<https://doi.org/10.1016/j.neuroimage.2018.05.046>.
- 829 Baum, G.L., Roalf, D.R., Cook, P.A., Ciric, R., Rosen, A.F., Xia, C., Elliott, M.A., Ruparel, K., Verma, R., Tunç, B., et al., 2018. The impact of in-scanner head motion on structural connectivity derived from diffusion mri. *Neuroimage* 173, 275–286.
- 833 Blesa, M., Sullivan, G., Anblagan, D., Telford, E.J., Quigley, A.J., Sparrow, S.A., Serag, A., Semple, S.I., Bastin, M.E., Boardman, J.P., 2019. Early breast milk exposure modifies brain connectivity in preterm infants. *NeuroImage* 184, 431 – 439. doi:<https://doi.org/10.1016/j.neuroimage.2018.09.045>.
- 838 Boardman, J., Craven, C., Valappil, S., Counsell, S., Dyet, L., Rueckert, D., Aljabar, P., Rutherford, M., Chew, A., Allsop, J., Cowan, F., Edwards, A.,



2010. A common neonatal image phenotype predicts adverse neurodevelopmental outcome in children born preterm. *NeuroImage* 52, 409 – 414. doi:<https://doi.org/10.1016/j.neuroimage.2010.04.261>.
- Boardman, J.P., Counsell, S.J., Rueckert, D., Kapellou, O., Bhatia, K.K., Aljabar, P., Hajnal, J., Allsop, J.M., Rutherford, M.A., Edwards, A.D., 2006. Abnormal deep grey matter development following preterm birth detected using deformation-based morphometry. *NeuroImage* 32, 70–78. doi:<https://doi.org/10.1016/j.neuroimage.2006.03.029>.
- Boardman, J.P., Walley, A., Ball, G., Takousis, P., Krishnan, M.L., Hughes-Carre, L., Aljabar, P., Serag, A., King, C., Merchant, N., Srinivasan, L., Froguel, P., Hajnal, J., Rueckert, D., Counsell, S., Edwards, A.D., 2014. Common genetic variants and risk of brain injury after preterm birth. *Pediatrics* 133, e1655–e1663. doi:10.1542/peds.2013-3011.
- Bonifacio, S.L., Glass, H.C., Chau, V., Berman, J.I., Xu, D., Brant, R., Barkovich, A.J., Poskitt, K.J., Miller, S.P., Ferriero, D.M., 2010. Extreme premature birth is not associated with impaired development of brain microstructure. *The Journal of Pediatrics* 157, 726–732.e1. doi:10.1016/J.JPEDI.2010.05.026.
- Bouyssi-Kobar, M., Brossard-Racine, M., Jacobs, M., Murnick, J., Chang, T., Limperopoulos, C., 2018. Regional microstructural organization of the cerebral cortex is affected by preterm birth. *NeuroImage: Clinical* 18, 871–880. doi:10.1016/j.nicl.2018.03.020.
- Brown, C.J., Miller, S.P., Booth, B.G., Andrews, S., Chau, V., Poskitt, K.J., Hamarneh, G., 2014. Structural network analysis of brain development in young preterm neonates. *NeuroImage* 101, 667 – 680. doi:<https://doi.org/10.1016/j.neuroimage.2014.07.030>.
- Brown, C.J., Moriarty, K.P., Miller, S.P., Booth, B.G., et al., 2017. Prediction of brain network age and factors of delayed maturation in very preterm

- infants, in: *Lecture Notes in Computer Science*, pp. 84–91. doi:10.1007/978-3-319-66182-7\_10.
- Brown, T., Kuperman, J., Chung, Y., Erhart, M., McCabe, C., Hagler, D., Venkatraman, V., Akshoomoff, N., Amaral, D., Bloss, C., Casey, B., Chang, L., Ernst, T., Frazier, J., Gruen, J., Kaufmann, W., Kenet, T., Kennedy, D., Murray, S., Sowell, E., Jernigan, T., Dale, A., 2012. Neuroanatomical Assessment of Biological Maturity. *Current Biology* 22, 1693–1698. doi:10.1016/J.CUB.2012.07.002.
- Caldinelli, C., Froudast-Walsh, S., Karolis, V., Tseng, C.E., Allin, M.P., Walshe, M., Cuddy, M., Murray, R.M., Nosarti, C., 2017. White matter alterations to cingulum and fornix following very preterm birth and their relationship with cognitive functions. *NeuroImage* 150, 373 – 382. doi:<https://doi.org/10.1016/j.neuroimage.2017.02.026>.
- Cao, M., Huang, H., He, Y., 2017. Developmental connectomics from infancy through early childhood. *Trends in neurosciences* 40, 494 – 506.
- Caruyer, E., Lenglet, C., Sapiro, G., Deriche, R., 2013. Design of multishell sampling schemes with uniform coverage in diffusion MRI. *Magnetic Resonance in Medicine* 69, 1534–1540. doi:10.1002/mrm.24736.
- Ceschin, R., Zahner, A., Reynolds, W., Gaesser, J., Zuccoli, G., Lo, C.W., Gopalakrishnan, V., Panigrahy, A., 2018. A computational framework for the detection of subcortical brain dysmaturation in neonatal MRI using 3D Convolutional Neural Networks. *NeuroImage* 178, 183–197. doi:10.1016/J.NEUROIMAGE.2018.05.049.
- Counsell, S.J., Edwards, A.D., Chew, A.T.M., Cowan, F.M., Boardman, J.P., Allsop, J.M., Hajnal, J.V., Srinivasan, L., Dyet, L.E., Rutherford, M.A., Anjari, M., 2008. Specific relations between neurodevelopmental abilities and white matter microstructure in children born preterm. *Brain* 131, 3201–3208.

- 895 Deprez, M., Wang, S., Ledig, C., Hajnal, J., Counsell, S., Schnabel, J., 2018.  
896 Segmentation of myelin-like signals on clinical MR images for age estimation  
897 in preterm infants. *bioRxiv* doi:10.1101/357749.
- 898 Dubois, J., Benders, M., Lazeyras, F., Borradori-Tolsa, C., Leuchter, R.H.V.,  
899 Mangin, J., Hüppi, P., 2010. Structural asymmetries of perisylvian regions in  
900 the preterm newborn. *NeuroImage* 52, 32–42. doi:10.1016/J.NEUROIMAGE.  
901 2010.03.054.
- 902 Duerden, E.G., Grunau, R.E., Guo, T., Foong, J., Pearson, A., Au-  
903 Young, S., Lavoie, R., Chakravarty, M.M., Chau, V., Synnes, A.,  
904 Miller, S.P., 2018. Early procedural pain is associated with regionally-  
905 specific alterations in thalamic development in preterm neonates.  
906 *Journal of Neuroscience* 38, 878–886. URL: [https://www.jneurosci.](https://www.jneurosci.org/content/38/4/878)  
907 [org/content/38/4/878](https://www.jneurosci.org/content/38/4/878), doi:10.1523/JNEUROSCI.0867-17.2017,  
908 [arXiv:https://www.jneurosci.org/content/38/4/878.full.pdf](https://www.jneurosci.org/content/38/4/878.full.pdf).
- 909 Duerden, E.G., Guo, T., Dodbiba, L., Chakravarty, M.M., Chau, V., Poskitt,  
910 K.J., Synnes, A., Grunau, R.E., Miller, S.P., 2016. Midazolam dose corre-  
911 lates with abnormal hippocampal growth and neurodevelopmental outcome in  
912 preterm infants. *Annals of Neurology* 79, 548–559. doi:10.1002/ana.24601.
- 913 Eaton-Rosen, Z., Melbourne, A., Orasanu, E., Cardoso, M.J., Modat, M., Bain-  
914 bridge, A., Kendall, G.S., Robertson, N.J., Marlow, N., Ourselin, S., 2015.  
915 Longitudinal measurement of the developing grey matter in preterm sub-  
916 jects using multi-modal MRI. *NeuroImage* 111, 580–589. doi:10.1016/J.  
917 NEUROIMAGE.2015.02.010.
- 918 Efron, B., 1983. Estimating the error rate of a prediction rule: improvement on  
919 cross-validation. *Journal of the American statistical association* 78, 316–331.
- 920 Genc, S., Malpas, C.B., Holland, S.K., Beare, R., Silk, T.J., 2017. Neurite  
921 density index is sensitive to age related differences in the developing brain.  
922 *NeuroImage* 148, 373–380. doi:10.1016/j.neuroimage.2017.01.023.

- 923 Glasser, M.F., Van Essen, D.C., 2011. Mapping human cortical areas in vivo  
924 based on myelin content as revealed by T1- and T2-Weighted MRI. *Journal*  
925 *of Neuroscience* 31, 11597–11616. doi:10.1523/JNEUROSCI.2180-11.2011.
- 926 Gousias, I.S., Edwards, A.D., Rutherford, M.A., Counsell, S.J., Hajnal, J.V.,  
927 Rueckert, D., Hammers, A., 2012. Magnetic resonance imaging of the newborn  
928 brain: Manual segmentation of labelled atlases in term-born and preterm  
929 infants. *NeuroImage* 62, 1499 – 1509. doi:[https://doi.org/10.1016/j.](https://doi.org/10.1016/j.neuroimage.2012.05.083)  
930 [neuroimage.2012.05.083](https://doi.org/10.1016/j.neuroimage.2012.05.083).
- 931 Greve, D.N., Fischl, B., 2009. Accurate and robust brain image alignment  
932 using boundary-based registration. *NeuroImage* 48, 63–72. doi:10.1016/j.  
933 [neuroimage.2009.06.060](https://doi.org/10.1016/j.neuroimage.2009.06.060).
- 934 Grussu, F., Schneider, T., Tur, C., Yates, R.L., Tachrount, M., Ianuş, A., Yian-  
935 nakas, M.C., Newcombe, J., Zhang, H., Alexander, D.C., et al., 2017. Neurite  
936 dispersion: a new marker of multiple sclerosis spinal cord pathology? *Annals*  
937 *of clinical and translational neurology* 4, 663–679.
- 938 Gui, L., Loukas, S., Lazeyras, F., Hüppi, P., Meskaldji, D., Borradori Tolsa, C.,  
939 2019. Longitudinal study of neonatal brain tissue volumes in preterm infants  
940 and their ability to predict neurodevelopmental outcome. *NeuroImage* 185,  
941 728–741. doi:10.1016/J.NEUROIMAGE.2018.06.034.
- 942 Hernandez-Fernandez, M., Reguly, I., Jbabdi, S., Giles, M., Smith, S.,  
943 Sotiropoulos, S.N., 2019. Using gpus to accelerate computational diffu-  
944 sion MRI: From microstructure estimation to tractography and connectomes.  
945 *NeuroImage* 188, 598 – 615. doi:[https://doi.org/10.1016/j.neuroimage.](https://doi.org/10.1016/j.neuroimage.2018.12.015)  
946 [2018.12.015](https://doi.org/10.1016/j.neuroimage.2018.12.015).
- 947 Hunter, J.D., 2007. Matplotlib: A 2d graphics environment. *Computing in*  
948 *science & engineering* 9, 90.
- 949 Jelescu, I.O., Veraart, J., Adisetiyo, V., Milla, S.S., Novikov, D.S.,  
950 Fieremans, E., 2015. One diffusion acquisition and different white

- 951 matter models: How does microstructure change in human early de-  
 952 velopment based on wmti and nodd? NeuroImage 107, 242  
 953 – 256. URL: [http://www.sciencedirect.com/science/article/pii/](http://www.sciencedirect.com/science/article/pii/S1053811914010015)  
 954 [S1053811914010015](http://www.sciencedirect.com/science/article/pii/S1053811914010015), doi:[https://doi.org/10.1016/j.neuroimage.2014.](https://doi.org/10.1016/j.neuroimage.2014.12.009)  
 955 [12.009](https://doi.org/10.1016/j.neuroimage.2014.12.009).
- 956 Jensen, J., Helpert, J., Ramani, A., Lu, H., Kaczynski, K., 2005. Diffusional  
 957 kurtosis imaging: The quantification of nongaussian water diffusion by means  
 958 of magnetic resonance imaging. Magnetic Resonance in Medicine 53, 1432–  
 959 1440. doi:10.1002/mrm.20508.
- 960 Job, D.E., Dickie, D.A., Rodriguez, D., Robson, A., Danso, S., Per-  
 961 net, C., Bastin, M.E., Boardman, J.P., Murray, A.D., Ahearn, T.,  
 962 Waiter, G.D., Staff, R.T., Deary, I.J., Shenkin, S.D., Wardlaw, J.M.,  
 963 2017. A brain imaging repository of normal structural mri across the  
 964 life course: Brain images of normal subjects (brains). NeuroImage 144,  
 965 299 – 304. URL: [http://www.sciencedirect.com/science/article/pii/](http://www.sciencedirect.com/science/article/pii/S1053811916000331)  
 966 [S1053811916000331](http://www.sciencedirect.com/science/article/pii/S1053811916000331), doi:[https://doi.org/10.1016/j.neuroimage.2016.](https://doi.org/10.1016/j.neuroimage.2016.01.027)  
 967 [01.027](https://doi.org/10.1016/j.neuroimage.2016.01.027). data Sharing Part II.
- 968 Jones, E., Oliphant, T., Peterson, P., et al., 2001. SciPy: Open source scientific  
 969 tools for Python,. <http://www.scipy.org/>.
- 970 Karmacharya, S., Gagoski, B., Ning, L., Vyas, R., Cheng, H.H., Soul, J., New-  
 971 berger, J.W., Shenton, M.E., Rathi, Y., Grant, P.E., 2018. Advanced diffu-  
 972 sion imaging for assessing normal white matter development in neonates and  
 973 characterizing aberrant development in congenital heart disease. NeuroImage:  
 974 Clinical 19, 360–373. doi:10.1016/j.nicl.2018.04.032.
- 975 Kellner, E., Dhital, B., Kiselev, V.G., Reiser, M., 2016. Gibbs-ringing artifact  
 976 removal based on local subvoxel-shifts. Magnetic Resonance in Medicine 76,  
 977 1574–1581. doi:10.1002/mrm.26054.
- 978 Keunen, K., Benders, M.J., Leemans, A., Fieret-Van Stam, P.C., Scholtens,  
 979 L.H., Viergever, M.A., Kahn, R.S., Groenendaal, F., de Vries, L.S., van den

- 980 Heuvel, M.P., 2017. White matter maturation in the neonatal brain is pre-  
 981 dictive of school age cognitive capacities in children born very preterm. *De-*  
 982 *velopmental Medicine & Child Neurology* 59, 939–946.
- 983 Kohavi, R., 1995. A study of cross-validation and bootstrap for accuracy esti-  
 984 mation and model selection, in: *Proceedings of the 14th international joint*  
 985 *conference on Artificial intelligence-Volume 2*, Morgan Kaufmann Publishers  
 986 Inc.. pp. 1137–1143.
- 987 Kostović, I., Jovanov-Milošević, N., 2006. The development of cerebral connec-  
 988 tions during the first 2045 weeks' gestation. *Seminars in Fetal and Neonatal*  
 989 *Medicine* 11, 415–422. doi:10.1016/J.SINY.2006.07.001.
- 990 Krishnan, M.L., Van Steenwinckel, J., Schang, A.L., Yan, J., Arnadottir, J.,  
 991 Le Charpentier, T., Csaba, Z., Dournaud, P., Cipriani, Constance Auvynet,  
 992 S., Titomanlio, L., Pansiot, J., Ball, G., Boardman, J.P., Walley, A.J., Saxena,  
 993 A., Mirza, G., Fleiss, B., Edwards, A.D., Petretto, E., Gressens, P., 2017.  
 994 Integrative genomics of microglia implicates *dlg4* (*psd95*) in the white matter  
 995 development of preterm infants. *Nature Communications* 8.
- 996 Krishnan, M.L., Wang, Z., Silver, M., Boardman, J.P., Ball, G., Coun-  
 997 sell, S.J., Walley, A.J., Montana, G., Edwards, A.D., 2016. Possible re-  
 998 lationship between common genetic variation and white matter develop-  
 999 ment in a pilot study of preterm infants. *Brain and behavior* 6, e00434.  
 1000 doi:10.1002/brb3.434.
- 1001 Krzywinski, M., Schein, J., Birol, I., Connors, J., Gascoyne, R., Horsman, D.,  
 1002 Jones, S.J., Marra, M.A., 2009. Circos: an information aesthetic for compar-  
 1003 ative genomics. *Genome research* 19, 1639–45. doi:10.1101/gr.092759.109.
- 1004 Kulikova, S., Hertz-Pannier, L., Dehaene-Lambertz, G., Buzmakov, A., Poupon,  
 1005 C., Dubois, J., 2015. Multi-parametric evaluation of the white matter  
 1006 maturation. *Brain Structure and Function* 220, 3657–3672. doi:10.1007/  
 1007 s00429-014-0881-y.

- 1008 Kunz, N., Zhang, H., Vasung, L., O'Brien, K.R., Assaf, Y., Lazeyras, F., Alexan-  
 1009 der, D.C., Hüppi, P.S., 2014. Assessing white matter microstructure of the  
 1010 newborn with multi-shell diffusion MRI and biophysical compartment models.  
 1011 *NeuroImage* 96, 288–299. doi:10.1016/j.neuroimage.2014.03.057.
- 1012 Leuchter, R.H.V., Gui, L., Poncet, A., Hagmann, C., Lodygensky, G.A., Martin,  
 1013 E., Koller, B., Darqu, A., Bucher, H.U., Hüppi, P.S., 2014. Association Between  
 1014 Early Administration of High-Dose Erythropoietin in Preterm Infants and  
 1015 Brain MRI Abnormality at Term-Equivalent Age. *JAMA* 312, 817–824.
- 1016 Li, W., Yang, C., Shi, F., Wu, S., Wang, Q., Nie, Y., Zhang, X., 2017. Construc-  
 1017 tion of individual morphological brain networks with multiple morphometric  
 1018 features. *Frontiers in Neuroanatomy* 11. doi:10.3389/fnana.2017.00034.
- 1019 Li, X., Morgan, P.S., Ashburner, J., Smith, J., Rorden, C., 2016. The first step  
 1020 for neuroimaging data analysis: Dicom to nifti conversion. *Journal of Neuro-*  
 1021 *science Methods* 264, 47 – 56. doi:https://doi.org/10.1016/j.jneumeth.  
 1022 2016.03.001.
- 1023 Mahjoub, I., Mahjoub, M.A., Rekik, I., 2018. Brain multiplexes reveal mor-  
 1024 phological connectional biomarkers fingerprinting late brain dementia states.  
 1025 *Scientific Reports* 8, 4103. doi:10.1038/s41598-018-21568-7.
- 1026 Makropoulos, A., Aljabar, P., Wright, R., Hüning, B., Merchant, N., et al., 2016.  
 1027 Regional growth and atlasing of the developing human brain. *NeuroImage*  
 1028 125, 456–478. doi:10.1016/j.neuroimage.2015.10.047.
- 1029 Makropoulos, A., Gousias, I.S., Ledig, C., Aljabar, P., Serag, A., Hajnal, J.V.,  
 1030 Edwards, A.D., Counsell, S.J., Rueckert, D., 2014. Automatic whole brain  
 1031 MRI segmentation of the developing neonatal brain. *IEEE Transactions on*  
 1032 *Medical Imaging* 33, 1818–1831. doi:10.1109/TMI.2014.2322280.
- 1033 Makropoulos, A., Robinson, E.C., Schuh, A., Wright, R., Fitzgibbon, S., et al.,  
 1034 2018. The developing human connectome project: A minimal processing

- 1035 pipeline for neonatal cortical surface reconstruction. *NeuroImage* 173, 88–  
1036 112. doi:10.1016/j.neuroimage.2018.01.054.
- 1037 Marcus, D., Harwell, J., Olsen, T., Hodge, M., Glasser, M., Prior, F., Jenkinson,  
1038 M., Laumann, T., Curtiss, S., Van Essen, D., 2011. Informatics and data  
1039 mining tools and strategies for the human connectome project. *Frontiers in*  
1040 *Neuroinformatics* 5, 4.
- 1041 Mathewson, K., Chow, C., Dobson, K., Pope, E., Schmidt, L., Van Lieshout,  
1042 R., 2017. Mental health of extremely low birth weight survivors: A systematic  
1043 review and meta-analysis. *Psychological Bulletin* 143, 347 – 383.
- 1044 Maximov, I.I., Alnaes, D., Westlye, L.T., 2019. Towards an optimised processing  
1045 pipeline for diffusion MRI data: Effects of artefact corrections on diffusion  
1046 metrics and their age associations in UK Biobank. *bioRxiv* .
- 1047 McKinney, W., et al., 2010. Data structures for statistical computing in python,  
1048 in: *Proceedings of the 9th Python in Science Conference*, Austin, TX. pp. 51–  
1049 56.
- 1050 Melbourne, A., Eaton-Rosen, Z., Orasanu, E., Price, D., Bainbridge, A., Car-  
1051 doso, M.J., Kendall, G.S., Robertson, N.J., Marlow, N., Ourselin, S., 2016.  
1052 Longitudinal development in the preterm thalamus and posterior white mat-  
1053 ter: MRI correlations between diffusion weighted imaging and T2 relaxome-  
1054 try. *Human Brain Mapping* 37, 2479–2492.
- 1055 Melbourne, A., Kendall, G.S., Cardoso, M.J., Gunny, R., Robertson, N.J., Mar-  
1056 low, N., Ourselin, S., 2014. Preterm birth affects the developmental synergy  
1057 between cortical folding and cortical connectivity observed on multimodal  
1058 MRI. *NeuroImage* 89, 23–34. doi:10.1016/J.NEUROIMAGE.2013.11.048.
- 1059 Nosarti, C., Reichenberg, A., Murray, R.M., Cnattingius, S., Lambe, M.P.,  
1060 Yin, L., MacCabe, J., Rifkin, L., Hultman, C.M., 2012. Preterm Birth and  
1061 Psychiatric Disorders in Young Adult Life. *Archives of General Psychiatry*  
1062 69, 610–617.



- 1063 Otsuka, Y., Chang, L., Kawasaki, Y., Wu, D., Ceritoglu, C., Oishi, K., Ernst,  
1064 T., Miller, M., Mori, S., Oishi, K., 2019. A multi-atlas label fusion tool for  
1065 neonatal brain mri parcellation and quantification. *Journal of Neuroimaging*  
1066 .
- 1067 Ouyang, M., Dubois, J., Yu, Q., Mukherjee, P., Huang, H., 2018. Delineation  
1068 of early brain development from fetuses to infants with diffusion MRI and  
1069 beyond. *NeuroImage* doi:10.1016/j.neuroimage.2018.04.017.
- 1070 Ouyang, M., Jeon, T., Sotiras, A., Peng, Q., Mishra, V., Halovanic, C., Chen,  
1071 M., Chalak, L., Rollins, N., Roberts, T.P.L., Davatzikos, C., Huang, H.,  
1072 2019. Differential cortical microstructural maturation in the preterm human  
1073 brain with diffusion kurtosis and tensor imaging. *Proceedings of the National*  
1074 *Academy of Sciences* , 201812156doi:10.1073/PNAS.1812156116.
- 1075 Pedregosa, F., Varoquaux, G., Gramfort, A., Michel, V., Thirion, B., Grisel, O.,  
1076 Blondel, M., Prettenhofer, P., Weiss, R., Dubourg, V., et al., 2011. Scikit-  
1077 learn: Machine learning in python. *Journal of machine learning research* 12,  
1078 2825–2830.
- 1079 Schneider, J., Fischer Fumeaux, C.J., Duerden, E.G., Guo, T., Foong, J.,  
1080 Graz, M.B., Hagmann, P., Chakravarty, M.M., Hüppi, P.S., Beauport, L.,  
1081 Truttmann, A.C., Miller, S.P., 2018. Nutrient intake in the first two weeks  
1082 of life and brain growth in preterm neonates. *Pediatrics* 141. doi:10.1542/  
1083 peds.2017–2169.
- 1084 Seabold, S., Perktold, J., 2010. Statsmodels: Econometric and statistical mod-  
1085 eling with python, in: *Proceedings of the 9th Python in Science Conference*,  
1086 *Scipy*. p. 61.
- 1087 Seidlitz, J., Váša, F., Shinn, M., Romero-Garcia, R., Whitaker, K.J., et al.,  
1088 2018. Morphometric similarity networks detect microscale cortical organiza-  
1089 tion and predict inter-individual cognitive variation. *Neuron* 97, 231–247.e7.  
1090 doi:10.1016/j.neuron.2017.11.039.

- 1091 Serag, A., Aljabar, P., Ball, G., Counsell, S.J., Boardman, J.P., Rutherford,  
1092 M.A., Edwards, A.D., Hajnal, J.V., Rueckert, D., 2012. Construction of a  
1093 consistent high-definition spatio-temporal atlas of the developing brain using  
1094 adaptive kernel regression. *NeuroImage* 59, 2255 – 2265. doi:[https://doi.](https://doi.org/10.1016/j.neuroimage.2011.09.062)  
1095 [org/10.1016/j.neuroimage.2011.09.062](https://doi.org/10.1016/j.neuroimage.2011.09.062).
- 1096 Shi, F., Yap, P.T., Gao, W., Lin, W., Gilmore, J.H., Shen, D., 2012. Altered  
1097 structural connectivity in neonates at genetic risk for schizophrenia: A com-  
1098 bined study using morphological and white matter networks. *NeuroImage* 62,  
1099 1622–1633. doi:[10.1016/j.neuroimage.2012.05.026](https://doi.org/10.1016/j.neuroimage.2012.05.026).
- 1100 Smith, S.M., 2002. Fast robust automated brain extraction. *Human Brain*  
1101 *Mapping* 17, 143–155. doi:[10.1002/hbm.10062](https://doi.org/10.1002/hbm.10062).
- 1102 Smith, S.M., Jenkinson, M., Woolrich, M.W., Beckmann, C.F., Behrens, T.E.,  
1103 Johansen-Berg, H., Bannister, P.R., Luca, M.D., Drobnjak, I., Flitney,  
1104 D.E., Niazy, R.K., Saunders, J., Vickers, J., Zhang, Y., Stefano, N.D.,  
1105 Brady, J.M., Matthews, P.M., 2004. Advances in functional and struc-  
1106 tural mr image analysis and implementation as fsl. *NeuroImage* 23, S208  
1107 – S219. doi:<https://doi.org/10.1016/j.neuroimage.2004.07.051>. math-  
1108 ematics in Brain Imaging.
- 1109 Smyser, C.D., Dosenbach, N.U., Smyser, T.A., Snyder, A.Z., Rogers, C.E.,  
1110 Inder, T.E., Schlaggar, B.L., Neil, J.J., 2016a. Prediction of brain maturity  
1111 in infants using machine-learning algorithms. *NeuroImage* 136, 1–9. doi:[10.](https://doi.org/10.1016/j.neuroimage.2016.05.029)  
1112 [1016/J.NEUROIMAGE.2016.05.029](https://doi.org/10.1016/j.neuroimage.2016.05.029).
- 1113 Smyser, T.A., Smyser, C.D., Rogers, C.E., Gillespie, S.K., Inder, T.E., Neil, J.J.,  
1114 2016b. Cortical gray and adjacent white matter demonstrate synchronous  
1115 maturation in very preterm infants. *Cerebral Cortex* 26, 3370–3378. doi:[10.](https://doi.org/10.1093/cercor/bhv164)  
1116 [1093/cercor/bhv164](https://doi.org/10.1093/cercor/bhv164).
- 1117 Soussia, M., Rekik, I., 2018. Unsupervised manifold learning using high-order  
1118 morphological brain networks derived from T1-w MRI for autism diagnosis.  
1119 *Frontiers in Neuroinformatics* 12, 70. doi:[10.3389/fninf.2018.00070](https://doi.org/10.3389/fninf.2018.00070).

- 1120 Sparrow, S., Manning, J.R., Cartier, J., Anblagan, D., Bastin, M.E., Piyasena,  
1121 C., Pataky, R., Moore, E.J., Semple, S.I., Wilkinson, A.G., Evans, M., Drake,  
1122 A.J., Boardman, J.P., 2016. Epigenomic profiling of preterm infants reveals  
1123 DNA methylation differences at sites associated with neural function. *Trans-*  
1124 *lational psychiatry* 6, e716. doi:10.1038/tp.2015.210.
- 1125 Steven, A.J., Zhuo, J., Melhem, E.R., 2014. Diffusion kurtosis imaging: an  
1126 emerging technique for evaluating the microstructural environment of the  
1127 brain. *AJR. American journal of roentgenology* 202 1, W26–33.
- 1128 Tariq, M., Schneider, T., Alexander, D.C., Wheeler-Kingshott, C.A.G., Zhang,  
1129 H., 2016. Bingham-NODDI: Mapping anisotropic orientation dispersion of  
1130 neurites using diffusion MRI. *NeuroImage* 133, 207 – 223. doi:[https://doi.](https://doi.org/10.1016/j.neuroimage.2016.01.046)  
1131 [org/10.1016/j.neuroimage.2016.01.046](https://doi.org/10.1016/j.neuroimage.2016.01.046).
- 1132 Telford, E.J., Cox, S.R., Fletcher-Watson, S., Anblagan, D., Sparrow, S.,  
1133 Pataky, R., Quigley, A., Semple, S.I., Bastin, M.E., Boardman, J.P., 2017.  
1134 A latent measure explains substantial variance in white matter microstruc-  
1135 ture across the newborn human brain. *Brain Structure and Function* 222,  
1136 4023–4033.
- 1137 Thompson, D.K., Chen, J., Beare, R., Adamson, C.L., Ellis, R., Ahmadzai,  
1138 Z.M., Kelly, C.E., Lee, K.J., Zalesky, A., Yang, J.Y., Hunt, R.W., Cheong,  
1139 J.L., Inder, T.E., Doyle, L.W., Seal, M.L., Anderson, P.J., 2016. Structural  
1140 connectivity relates to perinatal factors and functional impairment at 7years  
1141 in children born very preterm. *NeuroImage* 134, 328 – 337. doi:[https://](https://doi.org/10.1016/j.neuroimage.2016.03.070)  
1142 [doi.org/10.1016/j.neuroimage.2016.03.070](https://doi.org/10.1016/j.neuroimage.2016.03.070).
- 1143 Thompson, D.K., Kelly, C.E., Chen, J., Beare, R., Alexander, B., Seal, M.L.,  
1144 Lee, K., Matthews, L.G., Anderson, P.J., Doyle, L.W., Spittle, A.J., Cheong,  
1145 J.L., 2018a. Early life predictors of brain development at term-equivalent  
1146 age in infants born across the gestational age spectrum. *NeuroImage* doi:10.  
1147 1016/j.neuroimage.2018.04.031.

- 1148 Thompson, D.K., Kelly, C.E., Chen, J., Beare, R., Alexander, B., Seal, M.L.,  
1149 Lee, K.J., Matthews, L.G., Anderson, P.J., Doyle, L.W., Cheong, J.L., Spit-  
1150 tle, A.J., 2018b. Characterisation of brain volume and microstructure at  
1151 term-equivalent age in infants born across the gestational age spectrum. *Neu-*  
1152 *roImage: Clinical* , 101630.
- 1153 Toews, M., Wells, W.M., Zöllei, L., 2012. A feature-based developmental model  
1154 of the infant brain in structural MRI, in: *International Conference on Medical*  
1155 *Image Computing and Computer-Assisted Intervention*, Springer. pp. 204–  
1156 211.
- 1157 Toulmin, H., Beckmann, C.F., O’Muircheartaigh, J., Ball, G., Nongena, P.,  
1158 Makropoulos, A., Ederies, A., Counsell, S.J., Kennea, N., Arichi, T., Tu-  
1159 sor, N., Rutherford, M.A., Azzopardi, D., Gonzalez-Cinca, N., Hajnal, J.V.,  
1160 Edwards, A.D., 2015. Specialization and integration of functional thalamocor-  
1161 tical connectivity in the human infant. *Proceedings of the National Academy*  
1162 *of Sciences* 112, 6485–6490.
- 1163 Tournier, J.D., Smith, R.E., Raffelt, D.A., Tabbara, R., Dhollander, T., Pietsch,  
1164 M., Christiaens, D., Jeurissen, B., Yeh, C.H., Connelly, A., 2019. Mrtrix3: A  
1165 fast, flexible and open software framework for medical image processing and  
1166 visualisation. *bioRxiv* doi:10.1101/551739.
- 1167 Tustison, N.J., Avants, B.B., Cook, P.A., Zheng, Y., Egan, A., Yushkevich, P.A.,  
1168 Gee, J.C., 2010. N4ITK: Improved N3 bias correction. *IEEE Transactions on*  
1169 *Medical Imaging* 29, 1310–1320. doi:10.1109/TMI.2010.2046908.
- 1170 Van Den Heuvel, M.P., Kersbergen, K.J., De Reus, M.A., Keunen, K., et al.,  
1171 2015. The neonatal connectome during preterm brain development. *Cerebral*  
1172 *Cortex* 25, 3000–3013. doi:10.1093/cercor/bhu095.
- 1173 Van Der Walt, S., Colbert, S.C., Varoquaux, G., 2011. The numpy array:  
1174 a structure for efficient numerical computation. *Computing in Science &*  
1175 *Engineering* 13, 22.

- 1176 Van Lieshout, R.J., Ferro, M.A., Schmidt, L.A., Boyle, M.H., Saigal, S., Mor-  
 1177 rison, K.M., Mathewson, K.J., 2018. Trajectories of psychopathology in ex-  
 1178 tremely low birth weight survivors from early adolescence to adulthood: a  
 1179 20-year longitudinal study. *Journal of Child Psychology and Psychiatry* 59,  
 1180 1192–1200.
- 1181 Varoquaux, G., 2018. Cross-validation failure: small sample sizes lead to large  
 1182 error bars. *Neuroimage* 180, 68–77.
- 1183 Varoquaux, G., Raamana, P.R., Engemann, D.A., Hoyos-Idrobo, A., Schwartz,  
 1184 Y., Thirion, B., 2017. Assessing and tuning brain decoders: cross-validation,  
 1185 caveats, and guidelines. *NeuroImage* 145, 166–179.
- 1186 Veraart, J., Fieremans, E., Novikov, D.S., 2016. Diffusion MRI noise mapping  
 1187 using random matrix theory. *Magnetic Resonance in Medicine* 76, 1582–1593.  
 1188 doi:10.1002/mrm.26059.
- 1189 Veraart, J., Novikov, D.S., Christiaens, D., Ades-aron, B., Sijbers, J., Fiere-  
 1190 mans, E., 2016b. Denoising of diffusion MRI using random matrix theory.  
 1191 *NeuroImage* 142, 394–406. doi:10.1016/j.neuroimage.2016.08.016.
- 1192 Weiskopf, N., Suckling, J., Williams, G., Correia, M.M., Inkster, B., Tait, R.,  
 1193 Ooi, C., Bullmore, E.T., Lutti, A., 2013. Quantitative multi-parameter map-  
 1194 ping of R1, PD\*, MT, and R2\* at 3T: a multi-center validation. *Frontiers in*  
 1195 *Neuroscience* 7. doi:10.3389/fnins.2013.00095.
- 1196 Woodward, L.J., Anderson, P.J., Austin, N.C., Howard, K., Inder, T.E., 2006.  
 1197 Neonatal mri to predict neurodevelopmental outcomes in preterm infants.  
 1198 *New England Journal of Medicine* 355, 685–694.
- 1199 Wu, Z., Li, G., Shen, D., Hu, D., Lin, W., 2019. Hierarchical rough-to-fine  
 1200 model for infant age prediction based on cortical features. *IEEE Journal of*  
 1201 *Biomedical and Health Informatics* , 1–1doi:10.1109/jbhi.2019.2897020.

- 1202 Yap, P.T., Fan, Y., Chen, Y., Gilmore, J.H., Lin, W., Shen, D., 2011. Develop-  
1203 ment trends of white matter connectivity in the first years of life. PLoS ONE  
1204 6, e24678. doi:10.1371/journal.pone.0024678.
- 1205 Zhang, H., Schneider, T., Wheeler-Kingshott, C.A., Alexander, D.C., 2012.  
1206 NODDI: Practical in vivo neurite orientation dispersion and density imaging  
1207 of the human brain. NeuroImage 61, 1000–1016. doi:10.1016/j.neuroimage.  
1208 2012.03.072.
- 1209 Zou, H., Hastie, T., 2005. Regularization and variable selection via the elastic  
1210 net. Journal of the Royal Statistical Society: Series B (Statistical Methodol-  
1211 ogy) 67, 301–320.

**Credit Author Statement**

Paola Galdi: Conceptualization, Methodology, Software, Writing - Original Draft

Manuel Blesa: Conceptualization, Methodology, Software, Writing - Original Draft

David Q. Stoye: Resources, Data Curation, Writing - Review & Editing

Gemma Sullivan: Resources, Data Curation, Writing - Review & Editing

Gillian J. Lamb: Resources, Data Curation, Writing - Review & Editing

Alan J. Quigley: Resources, Data Curation, Writing - Review & Editing

Michael J. Thrippleton: Resources, Data Curation, Writing - Review & Editing

Mark E. Bastin: Resources, Data Curation, Writing - Review & Editing, Supervision

James P. Boardman: Resources, Writing - Review & Editing, Supervision, Funding acquisition